A micromechanics-based model for polycrystalline Ni–Ti wires

Philippe Hannequart, Michaël Peigney, Jean-François Caron

A Micromechanics-based Model for Polycrystalline Ni-Ti Wires

Philippe Hannequart[1,2], **Michaël Peigney**[1], **Jean-François Caron**[1]

[1] Université Paris-Est, Laboratoire Navier (Ecole des Ponts ParisTech, IFSTTAR, CNRS), F-77455 Marne-la-Vallée Cedex 2, France

[2] Arcora, Groupe Ingérop, Rueil-Malmaison, France

E-mail: michael.peigney@polytechnique.org

Abstract.

This paper proposes a constitutive model for polycrystalline shape memory alloy (SMA) wires arising from micromechanical arguments. The texture of the polycrystal is captured through the volume fractions and the maximal transformation strain in each crystalline orientation. As a result, the model is able to reproduce texture effects such as nonlinear hardening during phase transformation. An attractive feature of the proposed model is that closed-form expressions of the material response can be obtained for typical thermomechanical loadings of interest in SMA, such as cyclic traction at high temperature or thermal cycling at a fixed stress. Those analytical solutions are notably useful for identifying the constitutive parameters of the model. A temperature-controlled testing apparatus for SMA wires was developed for performing a reliable characterization of Nickel-Titanium wires. All model parameters have been identified by means of three tests: differential scanning calorimetry, isothermal traction test and thermal cycling at constant stress.

Keywords Shape memory alloy, wire, polycrystal, micromechanics, modelling, analytical solution

1. Introduction

The specific properties of shape memory alloys (such as the superelastic behavior and the shape memory effect) are the result of a diffusionless solid/solid phase transformation between different crystallographic structures (austenite and

martensite). From their discovery in the 1930s until today, shape memory alloys (SMA) have slowly become a widely used industrial material, with applications in various fields of engineering such as aeronautics, robotics, biomedicals or civil engineering. However, the great capabilities of this material are rarely fully exploited. For example, when the shape memory effect is used in actuators, there are often only two operating positions, a "cold" position and a "hot" position. The intermediary shapes of the SMA are rarely used. There are several possible reasons for this, such as the difficulty to manufacture the correct material, the nonlinear behaviour of SMAs (which makes it difficult to use simple control laws) and the lack of accurate thermomechanical models to correctly describe the phase change of SMAs.

A strong research effort has already been put into modeling of SMAs, both in the one-dimensional and three-dimensional settings. Roughly speaking, SMA models fall in two main categories: phenomenological macroscopic models and micromechanical models. Phenomenological macroscoping models draw inspiration from plasticity by using inelastic strains as internal variables [1, 2, 3, 4, 5, 6, 7]. In micromechanical models, the internal variables (usually the volume fractions of the different phases) are directly related to the austenite-martensite microstructures that develop in the material [8, 9, 10, 11, 12, 13, 14]. Compared to phenomenological models, micromechanical models provide more information on the material behavior: in addition to the macroscopic stress-strain-temperature relation, they also give some insight in the microstructures that appear at a microscopic scale. However, micromechanical models are more difficult to use and to implement in a finite-element code, partly because the number of internal variables is larger (and grows proportionally with the number of crystalline orientations). A third category of models that needs to mentioned is Landau/Landau-Ginzburg type models (see e.g. [15] and references therein). Those models are phenomelogical in nature, but they are able to describe the movements of martensite-martensite and austenite-martensite domain boundaries.

In a wide range of applications (such as actuators), SMAs are used in the form of wires loaded in tension. For such a simple geometry, the most widely used phenomenological models predict a piecewise linear response. This is in contradiction with experiments: for instance, experimental stress-strain curves at low temperature show some nonlinear hardening. It is possible to introduce nonlinear hardening in phenomenological models (as done in plasticity for instance), but this does not explain the physical original of that phenomenon. Numerical simulations based on

three-dimensional models [16] show that the origin of the nonlinear hardening lies in the polycrystalline nature of the material: Phase transformation initiates in grains which are the most favorably oriented with respect to the loading, and progressively extends to the least favorably oriented grains. The corresponding simulations are computationally intensive as they require to consider a large number of grains for capturing the nonlinear hardening in a convincing manner.

In this paper, our objective is to propose a micromechanical model of SMA wires that: (i) is able to capture the mechanical stress-induced nonlinear hardening in relation with the polycrystalline texture, (ii) remains of simple use, in the sense that closed-form solutions can be derived. To fulfill those objectives, we start from an already established three-dimensional micromechanical model and make use of the wire geometry to perform some simplification. This construction is detailed in Sect. 2. In the model obtained, the polycrystalline texture is taken into account via 2 scalar functions representing the volume fractions and the uniaxial transformation strain for each crystalline orientation. An attractive feature of the proposed model is that closed-form expressions of the material response can be obtained for typical thermomechanical loadings of interest in SMA, such as cyclic traction at high temperature (superelastic regime) or thermal cycling at a fixed stress. Those analytical solutions are presented in Sect. 3. In Sect. 4 are reported some experimental results from calorimetry tests, traction at fixed temperature, and thermal cycling at fixed stress. Those results are used to identify the material parameters and discuss the validity of the model.

2. Micromechanical modelling of polycrystalline SMA wires

2.1. Reversible model

The geometrically linear setting is adopted throughout the paper. Consider a reference single crystal of shape memory alloy and denote the three-dimensional transformation strains of the N martensitic variants by $\mathbf{e}_1^{tr}, \cdots, \mathbf{e}_N^{tr}$. These transformation strains are symmetry-related and have therefore the same trace k. They also verify the relation

$$\frac{1}{N}\sum_{i=1}^{N}\mathbf{e}_i^{tr} = k\mathbf{I} \tag{1}$$

where $\mathbf{I}$ is the identity second-order tensor. The value of k is very small for common shape memory alloys, which justifies using the approximation $k = 0$.

A polycrystalline SMA consists of numerous monocrystalline grains with distinct orientations. To each orientation corresponds a rotation $\mathbf{R}$ such that the transformation strains in the considered orientation are given by $\mathbf{R} \cdot \mathbf{e}_i^{tr} \cdot \mathbf{R}^T$ with $i = 1, \cdots, N$. Since the number of orientations can be very large, it is convenient to track the orientations with a continuously varying parameter s (which we can assume to vary in [0,1] without loss of generality). We denote by $\mathbf{R}(s)$ the rotation corresponding to orientation s. The transformation strains in orientation s are denoted by $\mathbf{e}_i^{tr}(s)$, i.e $\mathbf{e}_i^{tr}(s) = \mathbf{R}(s) \cdot \mathbf{e}_i^{tr} \cdot \mathbf{R}(s)^T$. We also introduce the volumic density $c(s)$ of orientation s. The function $c(s)$ is positive and satisfies

$$\int_0^1 c(s)ds = 1.$$

The functions $\mathbf{R}(s)$ and $c(s)$ capture some information on the texture of the polycrystal. In three-dimensional reversible models of polycrystalline shape memory alloys, a commonly used expression for the free energy is

$$W(\mathbf{e}, T) = \inf_{\Theta_1, \cdots, \Theta_N} W(\mathbf{e}, T, \Theta_1, \cdots, \Theta_N) \tag{2}$$

where

$$\begin{aligned} W(\mathbf{e}, T, \Theta_1, \cdots, \Theta_N) = \; & \frac{1}{2}(\mathbf{e} - \int_0^1 \sum_{i=1}^N \Theta_i(s)\mathbf{e}_i^{tr}(s)ds) : \mathbb{L} : (\mathbf{e} - \int_0^1 \sum_{i=1}^N \Theta_i(s)\mathbf{e}_i^{tr}(s)ds) \\ & + \lambda(T) \int_0^1 \sum_{i=1}^N \Theta_i(s)ds + m(T). \end{aligned} \tag{3}$$

In (2) and (3), $\mathbf{e}$ is the strain tensor, $\mathbb{L}$ is the elasticity tensor and $\lambda(T)$ is usually taken in the form

$$\lambda(T) = \frac{T - T_0}{T_0}\lambda_0 \tag{4}$$

where T_0 is the critical temperature of phase transition and λ_0 is the latent heat. A common expression of the term $m(T)$ in (3) is

$$m(T) = c(1 - \log \frac{T}{T_0})$$

where c is the specific heat [17].

Expression (3) rests on some assumptions. In particular, the elastic interaction between the individual austenite/martensite phases as well as the interaction between the grains are ignored. Those interactions would typically result in a additional mixing energy term in (3) (see e.g. [18, 19, 20] for some results in that direction). Expression (3) also ignores thermal strains which are supposed to remain small compared to transformation strains.In Eq. (3) it is also assumed that the austenite and the martensite have the elastic moduli: Such an assumption considerably simplifies the mathematical analysis but its validity remains questionable.

The scalar $\Theta_i(s)$ in (2) can be interpreted as the volume fraction of martensitic variant i in the grains with orientation s. Accordingly, the function $W(\varepsilon, T, \Theta_1, \cdots, \Theta_N)$ in (3) is referred to as the *free energy at fixed volume fractions*. In (2), the infimum is taken over the functions $\Theta_i(s)$ such that

$$\Theta_i(s) \geq 0, \ \sum_{i=1}^{N} \Theta_i(s) \leq c(s). \tag{5}$$

The stress-strain relation reads as $\boldsymbol{\sigma} = \partial W(\mathbf{e}, T)/\partial \mathbf{e}$, i.e.

$$\sigma = \mathbb{L} : \left(\mathbf{e} - \int_0^1 \sum_{i=1}^{N} \Theta_i(s) \mathbf{e}_i^{tr}(s) ds \right) \tag{6}$$

where $\Theta_i(s)$ is a solution to the minimization problem in (2).

Neglecting bending stiffness, the stress tensor $\boldsymbol{\sigma}$ in a wire is expected to be uniaxial with the form

$$\boldsymbol{\sigma} = \sigma \mathbf{n} \otimes \mathbf{n} \tag{7}$$

where $\mathbf{n}$ is a unit vector along the axis of the wire. Consider a infinitesimal element of length in which the stress is of the form (7). The strain $\mathbf{e}$ in the infinitesimal element is such that $\sigma \mathbf{n} \otimes \mathbf{n} = \partial W(\mathbf{e}, T)/\partial \mathbf{e}$ and therefore is a solution to the minimization problem

$$\inf_{\mathbf{e}} W(\mathbf{e}, T) - \sigma(\mathbf{n} \cdot \mathbf{e} \cdot \mathbf{n}). \tag{8}$$

Replacing W with its expression (2), the problem (8) becomes

$$\inf_{\mathbf{e}} \inf_{\Theta_1, \cdots, \Theta_N} W(\mathbf{e}, T, \Theta_1, \cdots, \Theta_N) - \sigma(\mathbf{n} \cdot \mathbf{e} \cdot \mathbf{n}). \tag{9}$$

where we recall from that the infimum is taken over volume fractions $\Theta_1, \cdots, \Theta_N$ satisfying (5). Swapping the two infima in (8) and calculating the infimum with respect to $\mathbf{e}$ yields

$$\mathbf{e} = \sigma \mathbb{L}^{-1} : (\mathbf{n} \otimes \mathbf{n}) + \int_0^1 \sum_{i=1}^{N} \Theta_i(s) \mathbf{e}_i^{tr}(s) ds. \tag{10}$$

Substituting (10) in (3) gives

$$W(\mathbf{e}, T, \Theta_1, \cdots, \Theta_N) - \sigma(\mathbf{n} \cdot \mathbf{e} \cdot \mathbf{n}) = \int_0^1 \sum_{i=1}^{N} \Theta_i(s)(\lambda(T) - \sigma(\mathbf{n} \cdot \mathbf{e}_i^{tr}(s) \cdot \mathbf{n}))ds + m(T).$$

The minimization problem (8) thus reduces to

$$\inf_{\Theta_1, \cdots, \Theta_N} \int_0^1 \sum_{i=1}^{N} \Theta_i(s)(\lambda(T) - \sigma(\mathbf{n} \cdot \mathbf{e}_i^{tr}(s) \cdot \mathbf{n}))ds \tag{11}$$

where the constant $m(T)$ has been dropped as it is independent of $\Theta_1, \cdots, \Theta_N$. In a way similar to (2) and (9), the infimum problem in (11) is restricted to volume fractions $\Theta_1, \cdots, \Theta_N$ satisfying the constraints (5).

In order to solve the linear program (11), it is convenient to relabel the transformation strains $\mathbf{e}_i^{tr}(s)$ of each orientation s in such a way that

$$\mathbf{n} \cdot \mathbf{e}_1^{tr}(s) \cdot \mathbf{n} \geq \mathbf{n} \cdot \mathbf{e}_2^{tr}(s) \cdot \mathbf{n} \geq \cdots \geq \mathbf{n} \cdot \mathbf{e}_N^{tr}(s) \cdot \mathbf{n} \tag{12}$$

In such an ordering, variant 1 can be interpreted as the most favorably oriented variant with respect to the loading direction. Except for very special values of the orientation matrix $\mathbf{R}(s)$, the inequalities in (12) are strict (which we assume in the following to simplify the presentation).

If $\sigma > 0$ (i.e. the wire is under tension), it can easily be verified that the volume fractions $\Theta_i(s)$ solutions to (11) satisfy

$$\Theta_i(s) = 0 \text{ for } i > 1 \tag{13}$$

i.e. the only martensitic variant that may appear in orientation s is the most favorably oriented one. If $\sigma = 0$ and $\lambda(T) \leq 0$, the minimum in (11) is attained for any set of volumes fractions such that $\sum_{i=1}^{N} \Theta_i(s) = c(s)$ for all s. Such volumes

fractions correspond to purely martensitic states. In particular, in view of (1), a self-accommodated state with negligible strain is obtained for

$$\Theta_i(s) = \frac{c(s)}{N}. \tag{14}$$

Self-accommodated states are typically observed when cooling down a stress-free specimen from a sufficiently high temperature.

In the model presented in this paper, we consider that the volume fractions $\Theta_i(s)$ are always linear combinations of states of the form (13) and (14), i.e. $\Theta_i(s)$ is assumed to be such that

$$\Theta_1(s) = \frac{1}{N}\theta_0(s) + \theta_1(s), \Theta_2(s) = \cdots = \Theta_N(s) = \frac{1}{N}\theta_0(s) \tag{15}$$

for some $\theta_0(s)$ that can be interpreted as the volume fraction of self-accommodated martensite. The scalars $\theta_0(s)$ and $\theta_1(s)$ are submitted to the constraints

$$\theta_0(s) \geq 0,\ \theta_1(s) \geq 0,\ \theta_0(s) + \theta_1(s) \leq c(s). \tag{16}$$

which are consistent with (5). For $\Theta_i(s)$ satisfying (15), the free energy in the infinitesimal element can be written as

$$W(\mathbf{e}, T, \Theta_1, \cdots, \Theta_N) = \frac{1}{2}\sigma^2(\mathbf{n}\otimes\mathbf{n}) : \mathbb{L}^{-1} : (\mathbf{n}\otimes\mathbf{n}) + \lambda(T)\int_0^1 (\theta_0(s)+\theta_1(s))ds + m(T) \tag{17}$$

where (10) has been used. Let

$$\varepsilon = \mathbf{n}\cdot\mathbf{e}\cdot\mathbf{n}$$

and

$$E = ((\mathbf{n}\otimes\mathbf{n}) : \mathbb{L}^{-1} : (\mathbf{n}\otimes\mathbf{n}))^{-1}$$

be respectively the strain and the elastic stiffness in the direction of the wire. Setting

$$\varepsilon^{tr}(s) = \mathbf{n}\cdot\mathbf{e}_1^{tr}(s)\cdot\mathbf{n} \tag{18}$$

and using (10), the expression (17) can be rewritten in terms of the uniaxial strain ε as

$$w(\varepsilon, T, \theta_0, \theta_1) = \frac{1}{2}E\left(\varepsilon - \int_0^1 \theta_1(s)\varepsilon^{tr}(s)ds\right)^2 + \lambda(T)\int_0^1 (\theta_0(s)+\theta_1(s))ds + m(T). \tag{19}$$

In the proposed model, we adopt Eq. (19) as the free energy at fixed volume fractions. Expression (19) is derived from the three-dimensional energy (3) by performing a model reduction based on the wire geometry. In particular, the number of internal variables has been reduced from N (equal to 12 for NiTi alloys) to 2. A list of the main symbols used in the model is supplied in Table 1.

Table 1. List of symbols for the model proposed

σ	uniaxial stress
ε	uniaxial strain
T	temperature
E	elastic modulus
$\lambda(T)$	latent heat at temperature T
T_0	critical temperature of phase transition
c	specific heat
s	continuous parameter (in $[0,1]$) tracking the crystalline orientations
$c(s)$	volume density of the crystalline orientation s
$\varepsilon^{tr}(s)$	transformation strain for the crystalline orientation s
f	inverse function of ε^{tr}
ε^{tr}_{min}	minimum value of the function $\varepsilon^{tr}(s)$
ε^{tr}_{max}	minimum value of the function $\varepsilon^{tr}(s)$
$\theta_0(s)$	volume fraction of self-accommodated martensite for the crystalline orientation s
$\theta_1(s)$	volume fraction of oriented martensite for the crystalline orientation s
G_0	Dissipative parameter for the self-accommodated (thermal induced) martensite
G_1	Dissipative parameter for the oriented (stress induced) martensite

A reversible model of SMA wire is obtained by minimizing (19) with respect to θ_0 and θ_1. The corresponding free energy reads as

$$w(\varepsilon, T) = \inf_{\theta_0,\theta_1} w(\varepsilon, T, \theta_0, \theta_1). \tag{20}$$

For later reference, we note that the Gibbs energy $w_*(\sigma, T) = \inf_\varepsilon w(\varepsilon, T) - \sigma\varepsilon$ corresponding to (20) is given by

$$w_*(\sigma, T) = \inf_{\theta_0(s),\theta_1(s)} w_*(\sigma, T, \theta_0, \theta_1) \tag{21}$$

with

$$w_*(\sigma, T, \theta_0, \theta_1) = -\frac{\sigma^2}{2E} - \sigma \int_0^1 \varepsilon^{tr}(s)\theta_1(s) + \lambda(T) \int_0^1 (\theta_0(s) + \theta_1(s))ds + m(T). \quad (22)$$

2.2. Dissipative model

Experiments show that irreversible effects (hysteresis) play an important role in SMAs. To capture such irreversible effects, we wish to appeal to the framework work of standard generalized materials [21], viewing (θ_0, θ_1) as internal variables and specifying their evolution law using a dissipation potential. In the classical framework of generalized standard materials (as applied for instance in hardening plasticity), the constitutive laws for a material with an internal variable α indeed read as

$$\sigma = \frac{\partial w}{\partial \varepsilon} \ , \ -\frac{\partial w}{\partial \alpha} \in \partial\Phi(\dot{\alpha}) \quad (23)$$

where Φ is the dissipation potential and ∂ is the subdifferential operator. Compared to hardening plasticity, a distinctive feature of phase transformation is that the internal variable (i.e. (θ_0, θ_1) in our case) is constrained. More specifically, (θ_0, θ_1) need to satisfy the inequalities (16) which result from mass conservation in the phase transformation process. In the presence of such constraints, the general constitutive laws (23) need to be amended as

$$\sigma = \frac{\partial w}{\partial \varepsilon} \ , \ -\frac{\partial w}{\partial \alpha} \in \partial\Phi(\dot{\alpha}) + \partial I_{\mathcal{T}}(\alpha) \quad (24)$$

where $I_{\mathcal{T}}$ is the indicator function associated to the constraints on the internal variable [22]. To be consistent with the second principle of thermodynamics, the dissipation potential Φ in (24) should be convex, positive and null at the origin. For the internal variable $\alpha = (\theta_0, \theta_1)$, the requirements on Φ are satisfied by the following function

$$\Phi(\dot{\theta}_0, \dot{\theta}_1) = \int_0^1 G_0|\dot{\theta}_0(s)| + G_1|\dot{\theta}_1(s)|ds \quad (25)$$

where G_0 and G_1 are positive parameters. We note that a similar dissipation potential has been used in [16, 8] in the 3D setting. As will be seen later in Sect. 3.2.1, consistency with the experimental observations on the phase transformation requires that

$$G_0 < G_1.$$

Adopting the expressions (19) for w and (25) for Φ, Eq. (24) yields the stress-strain relation

$$\sigma = E\left(\varepsilon - \int_0^1 \theta_1(s)\varepsilon^{tr}(s)ds\right) \tag{26}$$

and the evolution law

$$-\partial w \in \partial\Phi(\dot{\theta}_i) + \partial I_{\mathcal{T}}(\theta_0, \theta_1) \tag{27}$$

with

$$\partial w = (\frac{\partial w}{\partial \theta_0}, \frac{\partial w}{\partial \theta_1}) = (\lambda(T), \lambda(T) - \sigma\varepsilon^{tr}(s)). \tag{28}$$

In (27), the subdifferential $\partial\Phi(\dot{\theta}_i)$ is the multivalued operator given by

$$\partial\Phi(\dot{\theta}_i) = (B_0^d(s), B_1^d(s)) \tag{29}$$

with $B_i^d(s)$ satisfying

$$\begin{cases} |B_i^d(s)| \leq G_i & \text{if } \dot{\theta}_i(s) = 0 \\ B_i^d(s) = G_i & \text{if } \dot{\theta}_i(s) > 0 \\ B_i^d(s) = -G_i & \text{if } \dot{\theta}_i(s) < 0 \end{cases} \tag{30}$$

The subdifferential $\partial I_{\mathcal{T}}(\theta_0, \theta_1)$ is given by

$$\partial I_{\mathcal{T}}(\theta_0, \theta_1) = (z(s) - a_0(s), z(s) - a_1(s)) \tag{31}$$

with conditions

$$z(s) \geq 0, a_i(s) \geq 0, a_i(s)\theta_i(s) = 0, z(s)(c(s) - \theta_0(s) - \theta_1(s)) = 0. \tag{32}$$

Collecting the expressions above, the evolution law (27) becomes

$$\begin{aligned} -\lambda(T) &= B_0^d(s) + z(s) - a_0(s) \\ \sigma\varepsilon^{tr}(s) - \lambda(T) &= B_1^d(s) + z(s) - a_1(s) \end{aligned} \tag{33}$$

with conditions (30) and (32).

Consider a given local strain and temperature history $(\varepsilon(t), T(t))$ and denote by $\theta_i(s,t)$ the value of $\theta_i(s)$ at time t. Starting from a given initial state $\theta_i(s, t=0)$, the history $\theta_i(s,t)$ is found by solving the time evolution problem defined by Eqs (26), (30), (32) and (33). This task greatly simplifies in situations where $\theta_i(s,t)$ evolves monotonically with time. In such case, the values of $\theta_0(s,t)$ and $\theta_1(s,t)$ at any

given time t can indeed be obtained by solving the incremental energy minimization problem

$$\inf_{\theta_0,\theta_1} w(\varepsilon(t), T(t), \theta_i(s)) + \int_0^1 G_0\epsilon_0(s)\theta_0(s) + G_1\epsilon_1(s)\theta_1(s)ds \tag{34}$$

with $\epsilon_i(s) = 1$ if $\theta_i(s,t)$ is increasing with t and $\epsilon_i(s) = -1$ if $\theta_i(s,t)$ is decreasing. A justification of this result is provided in Appendix A. A similar result holds for stress controlled loadings: for a given local stress and temperature history $(\sigma(t), T(t))$ such that $\theta_i(s,t)$ evolves monotonically with time, the value of $\theta_0(s,t)$ and $\theta_1(s,t)$ at any given time t are a solution to the minimization problem

$$\inf_{\theta_0,\theta_1} w_*(\sigma(t), T(t), \theta_i(s)) + \int_0^1 G_0\epsilon_0(s)\theta_0(s) + G_1\epsilon_1(s)\theta_1(s)ds \tag{35}$$

where w_* is defined as in (22). We will make use of the incremental variational formulations (34) and (35) in the next section.

3. Analytical solutions

As detailed in the following, closed-form expressions of the response of the material can be obtained for typical loadings of interest for SMAs.

3.1. Traction at high temperature

3.1.1. Reversible case It is insightful to first consider the reversible model. For a prescribed strain ε, the state of the material is obtained by solving the minimization problem

$$\inf_{\theta_0,\theta_1} w(\varepsilon, T, \theta_0, \theta_1) \tag{36}$$

where θ_0 and θ_1 are submitted to the constraints (16). The stress σ is given by (26) where (θ_0, θ_1) is the solution of (36).

For solving (36) in the high temperature regime ($\lambda(T) \geq 0$), we first observe that $w(\varepsilon, T, \theta_0, \theta_1) > w(\varepsilon, T, 0, \theta_1)$ for any (θ_0, θ_1) satisfying (16) and such that $\theta_0 > 0$. It follows that the minimization problem (36) reduces to

$$\inf_{0\leq\theta_1(s)\leq c(s)} w(\varepsilon, T, 0, \theta_1) \tag{37}$$

i.e. there is no self-accommodated martensite in the energy-minimizing state. Writing down the local optimality conditions in (37) yields

$$-\sigma\varepsilon^{tr}(s) + \lambda(T) \begin{cases} = 0 & \text{if } \theta_1(s) \in (0, c(s)) \\ \geq 0 & \text{if } \theta_1(s) = 0 \\ \leq 0 & \text{if } \theta_1(s) = c(s) \end{cases} \tag{38}$$

If

$$\lambda(T) > \sigma\varepsilon^{tr}(s) \text{ for all } s \in [0,1] \tag{39}$$

then it follows from (38) that $\theta_1(s) = 0$ for all s, i.e. the material is in the purely austenitic phase. Similarly, if

$$\lambda(T) < \sigma\varepsilon^{tr}(s) \text{ for all } s \in [0,1] \tag{40}$$

then $\theta_1(s) = c(s)$ for all s, i.e. the material is purely in the oriented martensite phase. With proper labelling of the cristalline orientations, we can assume without loss of generality that $\varepsilon^{tr}(s)$ is a decreasing function of s. Setting $\varepsilon^{tr}_{max} = \varepsilon^{tr}(0)$ and $\varepsilon^{tr}_{min} = \varepsilon^{tr}(1)$, the conditions (39) and (40) thus translate as $\lambda(T) > \sigma\varepsilon^{tr}_{max}$ and $\lambda(T) < \sigma\varepsilon^{tr}_{min}$, respectively.

In the intermediary case where $\lambda(T)/\varepsilon^{tr}_{max} \leq \sigma \leq \lambda(T)/\varepsilon^{tr}_{min}$, the conditions (38) show that

$$\theta_1(s) = \begin{cases} c(s) & \text{for } s \leq s^*, \\ 0 & \text{for } s > s^* \end{cases} \tag{41}$$

where s^* is given by the consistency condition $-\sigma\varepsilon^{tr}(s^*) + \lambda(T) = 0$, i.e.

$$\lambda(T) = E\varepsilon^{tr}(s^*) \left(\varepsilon - \int_0^{s^*} c(s)\varepsilon^{tr}(s)ds \right) \tag{42}$$

Let us now detail the explicit expression of the stress-strain curve provided by the model. The most natural way to parameterize the stress-strain curve is to use ε as a parameter, solving (42) for each given ε and substituting the result in (26). This turns out to be a relatively complex calculation, even for simple functions $\varepsilon^{tr}(s)$ and $c(s)$. Such difficulties can be avoided if ε^{tr} is *strictly* decreasing, which we assume from now. In such case, the stress-strain curve is strictly increasing and can therefore by parameterized by σ. Denoting by f the inverse function of ε^{tr}, Eq. (42) can be equivalently rewritten as

$$s^* = f\left(\frac{\lambda(T)}{\sigma}\right). \tag{43}$$

From (26) and (41) we have

$$\varepsilon = \frac{\sigma}{E} + \int_0^{s^*} c(s)\varepsilon^{tr}(s)ds.$$

Using the change of variable $s = f(x)$ in the above integral yields

$$\varepsilon = \frac{\sigma}{E} + \int_{\varepsilon^{tr}_{max}}^{\lambda(T)/\sigma} f'(x)c(f(x))xdx \tag{44}$$

where (43) has been used. The relation (44) holds for $\lambda(T)/\varepsilon^{tr}_{max} \leq \sigma \leq \lambda(T)/\varepsilon^{tr}_{min}$ and gives the stress-strain response during phase transformation.

It is insightful to calculate the tangent stiffness $d\sigma/d\varepsilon$ during phase transformation. By differentiation of (42) and (44) we find

$$\frac{d\sigma}{d\varepsilon} = \frac{E}{1 - E\dfrac{\lambda(T)^2}{\sigma^3} f'(\dfrac{\lambda(T)}{\sigma})c(f(\dfrac{\lambda(T)}{\sigma}))} \tag{45}$$

Since ε^{tr} (and consequently f) is a decreasing function, it is clear from (45) that $0 \leq d\sigma/d\varepsilon \leq E$, i.e. the tangent stiffness is positive (there is no softening) and always remains smaller than the Young modulus of the pure phases. Eq. (45) shows that the tangent stiffness $d\sigma/d\varepsilon$ is a function of σ, meaning that the response of the material is nonlinear during phase transformation.

Table 2. Examples of function $\varepsilon^{tr}(s)$

Texture	function $\varepsilon^{tr}(s)$	Inverse function $f(x)$
A	$(\varepsilon^{tr}_{max} - \varepsilon^{tr}_{min})(1-s)^3 + \varepsilon^{tr}_{min}$	$1 - \left(\dfrac{x - \varepsilon^{tr}_{min}}{\varepsilon^{tr}_{max} - \varepsilon^{tr}_{min}}\right)^{\frac{1}{3}}$
B	$(\varepsilon^{tr}_{max} - \varepsilon^{tr}_{min}) \cos\left(\dfrac{\pi s}{2}\right) + \varepsilon^{tr}_{min}$	$\dfrac{2}{\pi} \arccos\left(\dfrac{x - \varepsilon^{tr}_{min}}{\varepsilon^{tr}_{max} - \varepsilon^{tr}_{min}}\right)$

Details of the stress-strain curve (44) depend on the functions ε^{tr} and c which capture some information on the texture of the polycrystalline material. As an illustration, some stress-strain curves are plotted in Fig.1 for two different textures

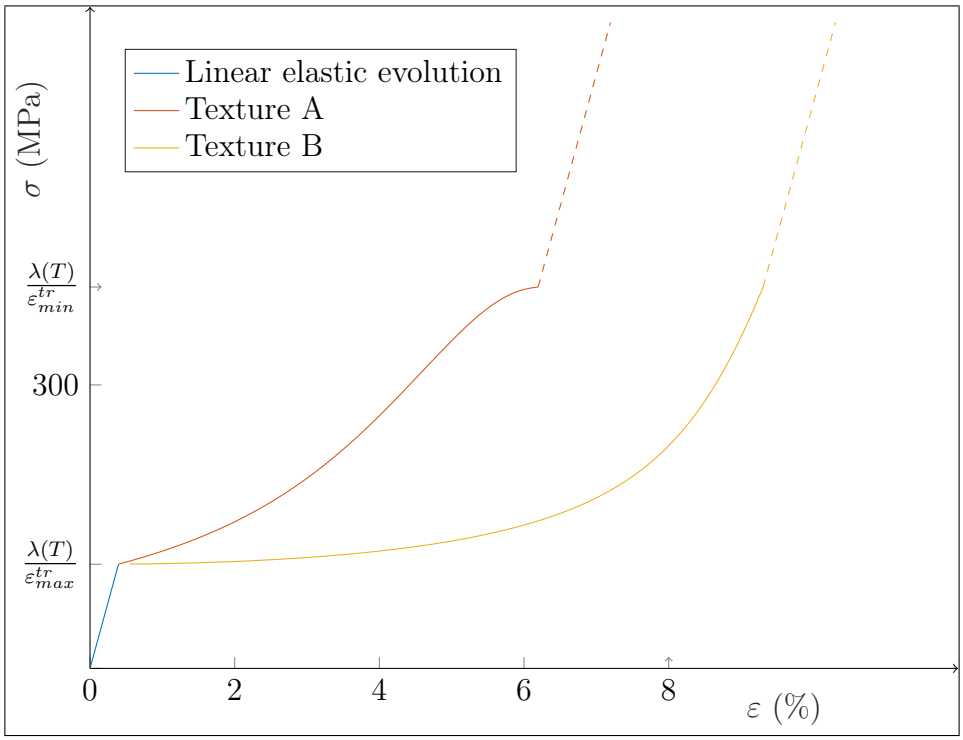

Figure 1. Superelastic stress-strain curves for the textures A and B, in the reversible case (no dissipation).

labelled as A and B. The corresponding $\varepsilon^{tr}(s)$ functions are listed in Table 2 and plotted in Fig. 2. The values $\varepsilon^{tr}_{min} = 0.03$, $\varepsilon^{tr}_{max} = 0.11$, $\lambda(T) = 12$ MPa, $E = 28$ GPa, $c(s) = 1$ have been used in Figs. 1 and 2.

In the case of textures A and B, the integral in (44) can be calculated in closed-form, leading to fully explicit expressions of the stress-strain response during phase transformation. The obtained expressions read as

$$\varepsilon = \frac{\sigma}{E} + \frac{1}{4}\left(\varepsilon^{tr}_{max} + 3\varepsilon^{tr}_{min} - \left(\frac{\frac{\lambda(T)}{\sigma} - \varepsilon^{tr}_{min}}{\varepsilon^{tr}_{max} - \varepsilon^{tr}_{min}}\right)^{\frac{1}{3}}\left(3\varepsilon^{tr}_{min} + \frac{\lambda(T)}{\sigma}\right)\right)$$

for texture A, and

$$\varepsilon = \frac{\sigma}{E} + \varepsilon^{tr}_{min} + \frac{2}{\pi}\Bigg[\sqrt{(\varepsilon^{tr}_{max} - \tfrac{\lambda(T)}{\sigma})(\varepsilon^{tr}_{max} - 2\varepsilon^{tr}_{min} + \tfrac{\lambda(T)}{\sigma})} \\ -\varepsilon^{tr}_{min} \arctan\left(\frac{\frac{\lambda(T)}{\sigma} - \varepsilon^{tr}_{min}}{\sqrt{(\varepsilon^{tr}_{max} - \frac{\lambda(T)}{\sigma})(\varepsilon^{tr}_{max} - 2\varepsilon^{tr}_{min} + \frac{\lambda(T)}{\sigma})}} \right) \Bigg]$$

for texture B.

As can be observed in Fig.1, the first elastic part of the stress-strain curves is the same for textures A and B. Then, once the threshold stress $\lambda(T)/\varepsilon^{tr}_{max}$ is exceeded, the curves present different evolutions. We note that depending on $\varepsilon^{tr}(s)$, the stress-strain curve can present sharp slope changes or smooth changes, at the beginning and at the end of phase transformation. The stresses at the beginning and at the end of phase transformation only depend on the function ε^{tr} through its extreme values ε^{tr}_{max} and ε^{tr}_{min}. A similar remark holds for the strain at the beginning of phase transformation. The strain at the end of phase transformation depends on the integral of $\varepsilon^{tr}(s)$ and is equal to

$$\frac{\lambda(T)}{E\varepsilon^{tr}_{max}} + \int_0^1 \varepsilon^{tr}(s)ds.$$

The term $\int_0^1 \varepsilon^{tr}(s)ds$ can be interpreted as the maximum recoverable strain of the wire. It is equal to $(\varepsilon^{tr}_{max} + 3\varepsilon^{tr}_{min})/4$ for texture A and $2(\varepsilon^{tr}_{max} - \varepsilon^{tr}_{min})/\pi + \varepsilon^{tr}_{min}$ for texture B. At the end of phase transformation, which occurs for $\sigma = \lambda(T)/\varepsilon^{tr}_{min}$, the evolution becomes linear elastic again, which is represented by dotted lines in Figure 1.

3.1.2. Dissipative case Let us now study how the results are modified in the dissipative case. We assume that the material is fully austenitic in the initial state, i.e. $\theta_0(s) = \theta_1(s) = 0$ for all s. An increasing strain ε is applied at a fixed temperature T such that $\lambda(T) > G_1$. For any given s, it is expected that $\theta_i(s)$ increases with the applied strain, as in the reversible case. The exact value of $\theta_i(s)$ can be obtained by using the variational formulation of the incremental evolution problem (34), which in the present case specializes as

$$\inf_{\theta_0,\theta_1} w(\varepsilon, T(t), \theta_0, \theta_1) + \int_0^1 G_0\theta_0(s) + G_1\theta_1(s)ds. \tag{46}$$

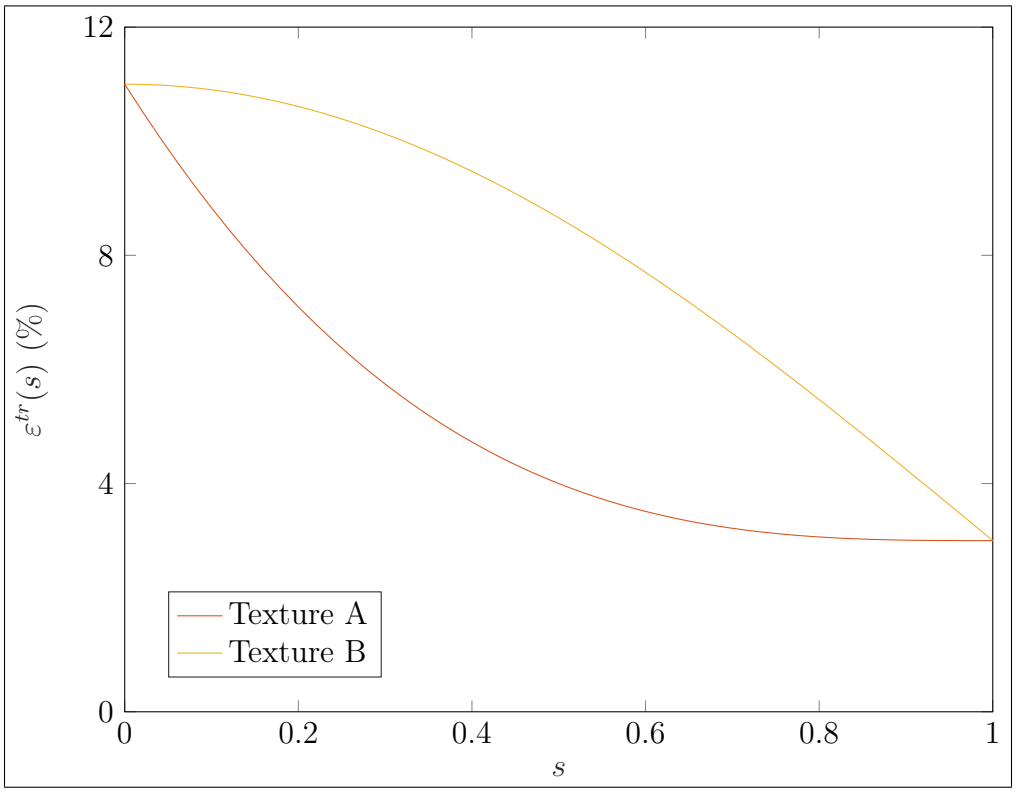

Figure 2. Examples of functions $\varepsilon^{tr}(s)$

An important observation is that (46) has the same structure as the minimization problem (36) considered in Sect. 3.1.1. It follows that the solution to (46) is obtained by replacing $\lambda(T)$ with $\lambda(T)+G_1$ in the expressions of the stress-strain response found previously in Sect. 3.1.1. We thus have

$$\begin{cases} \varepsilon = \dfrac{\sigma}{E} & \text{for } 0 \leq \sigma \leq \frac{\lambda(T)+G_1}{\varepsilon^{tr}_{max}} \\ \varepsilon = \dfrac{\sigma}{E} + \displaystyle\int_{\varepsilon^{tr}_{max}}^{\frac{\lambda(T)+G_1}{\sigma}} f'(x)c(f(x))xdx & \text{for } \frac{\lambda(T)+G_1}{\varepsilon^{tr}_{max}} \leq \sigma \leq \frac{\lambda(T)+G_1}{\varepsilon^{tr}_{min}} \\ \varepsilon = \dfrac{\sigma}{E} + \displaystyle\int_{\varepsilon^{tr}_{max}}^{\varepsilon^{tr}_{min}} f'(x)c(f(x))xdx & \text{for } \frac{\lambda(T)+G_1}{\varepsilon^{tr}_{min}} \leq \sigma \end{cases} \tag{47}$$

Eq. (47) give the stress-strain relations during loading, provided that $\lambda(T)+G_1 > 0$.

Let us now assume that the applied strain ε decreases after having reached a

maximum value ε^{max}. We denote by θ_1^{max} be the value of θ_1 when $\varepsilon = \varepsilon^{max}$. When ε decreases, it can be verified from the optimality conditions (33) that θ_i does not evolve as long as $\sigma\varepsilon^{tr}_{min} \geq \lambda(T) - G_1$. This corresponds to elastic unloading. For smaller values of σ, reverse phase transformation takes place, i.e. the volume fractions of martensite decrease. The problem (34) thus specializes as

$$\inf_{\theta_0,\theta_1} w(\varepsilon, T, \theta_0, \theta_1) - \int_0^1 (G_0\theta_0(s) + G_1\theta_1(s))ds. \tag{48}$$

Provided $\lambda(T) - G_1 > 0$, the minimization problem (48) has the same structure as (36) so that the solution to (48) is obtained by substituting $\lambda(T)$ with $\lambda(T) - G_1$ in the expressions obtained in Sect. 3.1.1. In summary, we have

$$\begin{cases} \varepsilon = \dfrac{\sigma}{E} & \text{for } 0 \leq \sigma \leq \frac{\lambda(T)-G_1}{\varepsilon^{tr}_{max}} \\ \varepsilon = \dfrac{\sigma}{E} + \displaystyle\int_{\varepsilon^{tr}_{max}}^{\frac{\lambda(T)-G_1}{\sigma}} f'(x)c(f(x))xdx & \text{for } \frac{\lambda(T)-G_1}{\varepsilon^{tr}_{max}} \leq \sigma \leq \frac{\lambda(T)-G_1}{\varepsilon^{tr}_{min}} \\ \varepsilon = \dfrac{\sigma}{E} + \displaystyle\int_0^1 \theta_1^{max}(s)\varepsilon^{tr}(s)ds & \text{for } \frac{\lambda(T)-G_1}{\varepsilon^{tr}_{min}} \leq \sigma \end{cases} \tag{49}$$

Eq. (49) give the stress-strain relations during unloading, provided that $\lambda(T) - G_1 > 0$. Such values of the temperature correspond to the superelastic regime of the material. In Fig.3 is presented an example of stress-strain cycle as provided by Eqs (47) and (49), using texture B with parameters $\varepsilon^{tr}_{max} = 0.11$, $\varepsilon^{tr}_{min} = 0.03$, $\lambda(T) = 12$ MPa, $E = 28$ GPa, $G_1 = 3$ MPa.

3.2. Thermal cycling under constant stress

Let us now consider a cyclic thermal loading at a constant stress σ. We assume that the material is fully austenitic in the initial state. During cooling, the volume fractions $\theta_i(s)$ increase so that the minimization problem (35) becomes

$$\inf_{\theta_0,\theta_1} -\sigma \int_0^1 \varepsilon^{tr}(s)\theta_1(s) + \lambda(T)\int_0^1 (\theta_0(s) + \theta_1(s))ds + \int_0^1 G_0\theta_0(s) + G_1\theta_1(s). \tag{50}$$

It can be checked from (50) that the evolution is elastic as long $\lambda(T) \geq \min(-G_0, \sigma\varepsilon^{tr}_{max} - G_1)$. The subsequent evolution depends on the value of the imposed stress σ, as detailed next.

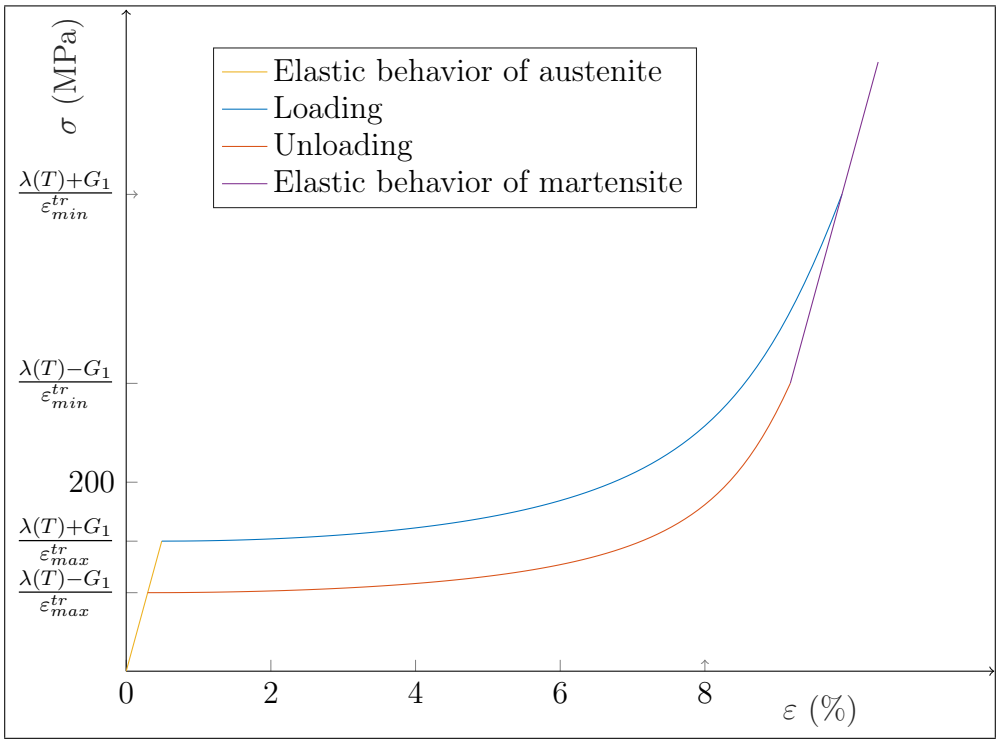

Figure 3. Example of superelastic response in the dissipative case - Texture B

3.2.1. Case $\sigma \leq (G_1 - G_0)/\varepsilon^{tr}_{max}$ Let us first consider the case where $\sigma \leq (G_1 - G_0)/\varepsilon^{tr}_{max}$. During cooling, the evolution is found to be elastic for $\lambda(T) > -G_0$. For $\lambda(T) \leq -G_0$, the solution to (50) is found to be given by $\theta_0(s) = c(s)$ for all s.

Assume now that the material is cooled down to a temperature such that $\lambda(T) < -G_0$ and subsequently heated. It can be verified that the solution to (50) is given by $\theta_0(s) = c(s), \theta_1 = 0$ as long as $\lambda(T) < G_0$, and that $\theta_0(s) = \theta_1 = 0$ for $\lambda(T) > G_0$, i.e. phase transformation in austenite occurs brutally at $\lambda(T) = G_0$.

This evolution scenario holds provided $\sigma \leq (G_1 - G_0)/\varepsilon^{tr}_{max}$, i.e. for sufficiently small values of the applied stress. Since $G_1 > G_0$, this evolution holds in particular for $\sigma = 0$, i.e. under stress-free condition.

3.2.2. Case $(G_1 - G_0)/\varepsilon^{tr}_{max} < \sigma < (G_1 - G_0)/\varepsilon^{tr}_{min}$ The cooling is found to be elastic as long as $\lambda(T) > \sigma\varepsilon^{tr}_{max} - G_1$. When $\lambda(T)$ reaches the critical value $\sigma\varepsilon^{tr}_{max} - G_1$, it

can be checked that the solution to (50) is given by

$$\begin{array}{ll} \theta_0(s) = 0, \theta_1(s) = c(s) & \text{for } s \leq f(\frac{G_1+\lambda(T)}{\sigma}) \\ \theta_0(s) = \theta_1(s) = 0 & \text{for } s > f(\frac{G_1+\lambda(T)}{\sigma}) \end{array} \tag{51}$$

Accordingly the strain ε is given by

$$\varepsilon = \frac{\sigma}{E} + \int_{\varepsilon^{tr}_{max}}^{\frac{G_1+\lambda(T)}{\sigma}} f'(x)c(f(x))xdx. \tag{52}$$

These results can be interpreted as phase transformation into oriented-martensite in the most favorable orientations. The solution (51) holds as long $\lambda(T) > -G_0$. For $\lambda(T) < -G_0$, the solution to (50) can be verified to be given by

$$\begin{array}{ll} \theta_0(s) = 0, \theta_1(s) = c(s) & \text{for } s \leq f(\frac{G_1-G_0}{\sigma}) \\ \theta_0(s) = c(s), \theta_1(s) = 0, & \text{for } s > f(\frac{G_1-G_0}{\sigma}) \end{array} \tag{53}$$

so that

$$\varepsilon = \frac{\sigma}{E} + \int_{\varepsilon^{tr}_{max}}^{\frac{G_1-G0}{\sigma}} f'(x)c(f(x))xdx \tag{54}$$

The results (53) mean the material state is a mixture of oriented martensite and self-accommodated martensite.

Assume now that the material is cooled down to a temperature such that $\lambda(T) < -G_0$ and subsequently heated. Omitting the detail of the calculation, the following evolution is obtained:

- for $\lambda(T) \leq G_0$, the evolution is elastic, i.e. θ_0, θ_1 and ε are given by (53) and (54).
- for $G_0 < \lambda(T) \leq 2G_1 - G_0$, the strain is given by (54) and θ_0, θ_1 are given by

$$\begin{array}{ll} \theta_0(s) = \theta_1(s) = 0 & \text{for } s > f(\frac{G_1-G_0}{\sigma}) \\ \theta_0(s) = 0, \theta_1(s) = c(s) & \text{for } s \leq f(\frac{G_1-G_0}{\sigma}) \end{array} \tag{55}$$

- for $2G_1 - G_0 < \lambda(T) \leq G_1 + \sigma\varepsilon^{tr}_{max}$, θ_0, θ_1 and ε are given by

$$\begin{array}{ll} \theta_0(s) = \theta_1(s) = 0 & \text{for } s > f(\frac{-G_1+\lambda(T)}{\sigma}) \\ \theta_0(s) = 0, \theta_1(s) = c(s) & \text{for } s \leq f(\frac{-G_1+\lambda(T)}{\sigma}) \\ \varepsilon = \dfrac{\sigma}{E} + \displaystyle\int_{\varepsilon^{tr}_{max}}^{\frac{-G_1+\lambda(T)}{\sigma}} f'(x)c(f(x))xdx & \end{array} \tag{56}$$

- for $G_1+\sigma\varepsilon^{tr}_{max} < \lambda(T)$, we have $\theta_0(s) = \theta_1(s) = 0$ and $\varepsilon = \sigma/E$, i.e. the material is fully in the austenitic phase.

3.2.3. Case $\sigma > (G_1 - G_0)/\varepsilon^{tr}_{min}$ As in the preceding case, the cooling is elastic as long as $\lambda(T) > \sigma\varepsilon^{tr}_{max} - G_1$. When $-\lambda(T)$ reaches the critical value $G_1 - \sigma\varepsilon^{tr}_{max}$, the solution to (50) is given by (51), i.e. phase transformation into oriented-martensite occurs in the most favorable orientations. In contrast with the preceding case, the solution (51) holds as long $\lambda(T) > \sigma\varepsilon^{tr}_{min} - G_1$. For $\lambda(T) < \sigma\varepsilon^{tr}_{min} - G_1$, the solution to (50) is given by $\theta_1(s) = c(s)$ for all s, i.e. all the grains are transformed in oriented martensite. Accordingly the strain ε is equal to $\sigma/E + \int_{\varepsilon^{tr}_{min}}^{\varepsilon^{tr}_{max}} c(s)\varepsilon^{tr}(s)ds$.

Omitting the detail of the calculation, the following evolution is obtained during heating from a temperature such that $\lambda(T) < \sigma\varepsilon^{tr}_{min} - G_1$:

- for $\lambda(T) \leq G_1 + \sigma\varepsilon^{tr}_{min}$, the evolution is elastic, i.e. $\theta_1(s) = c(s)$ and
$$\varepsilon = \sigma/E + \int_{\varepsilon^{tr}_{min}}^{\varepsilon^{tr}_{max}} c(s)\varepsilon^{tr}(s)ds$$
- for $G_1 + \sigma\varepsilon^{tr}_{min} < \lambda(T) \leq G_1 + \sigma\varepsilon^{tr}_{max}$, θ_0, θ_1 and ε are given (56).
- for $G_1 + \sigma\varepsilon^{tr}_{max} < \lambda(T)$, we have $\theta_0(s) = \theta_1(s) = 0$ and $\varepsilon = \sigma/E$, i.e. the material is fully in the austenitic phase.

In contrast with the case covered in Sect. 3.2.2, it can be observed that $\theta_0 = 0$ during the whole cycle, i.e. self-accommodated martensite never appears.

Three thermal cycles at constant stress corresponding to the three cases 3.2.1,3.2.2,3.2.3 are represented in Figure 4 for the texture B. Values of the parameters are $\varepsilon^{tr}_{min} = 0.01$, $\varepsilon^{tr}_{max} = 0.17$, $G_1 = 4$ MPa, $G_0 = 3.2$ MPa, $E = 28$ GPa. The term $\lambda(T)$ is taken in the form (4) with $\lambda_0 = 74.2$ MPa and $T_0 = 294.9$ K.

The first case (dotted curve in Figure 4) corresponds to an imposed stress which is too low to trigger phase transformation into oriented martensite during cooling. As a result, there is no change in the macroscopic strain.

The second case (solid curve in Figure 4) corresponds to an intermediary stress : the wire stretches during cooling and shrinks during heating. Note the temperature T at the end of phase transformation during cooling verifies $\lambda(T) = G_0$ and therefore is independent of the applied stress σ. A similar remarks holds for the temperature at the beginning of phase transformation during heating. The variation $\Delta\varepsilon$ of the strain between the cool state and the hot state is given by

$$\int_{\varepsilon^{tr}_{max}}^{\frac{G_1-G_0}{\varepsilon^{tr}_{max}}} f'(x)xdx \tag{57}$$

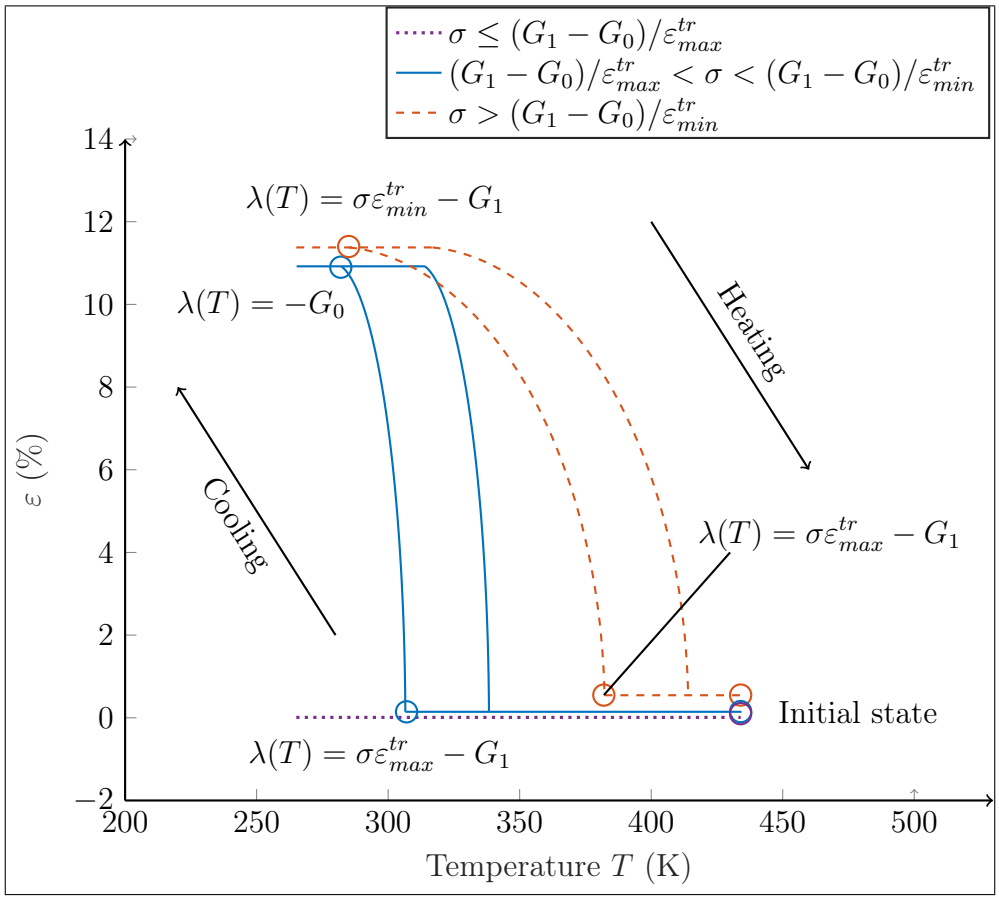

Figure 4. Thermal cycling at constant stress

and therefore increases with the applied constant stress σ. The value $\Delta\varepsilon$ in (57) is always smaller than the maximum recoverable strain $\int_0^1 \varepsilon^{tr}(s)ds$.

The third (dashed curve in Figure 4) corresponds to a high applied stress σ. Both during heating and cooling, the temperatures at beginning and end of phase transformation increase. The variation $\Delta\epsilon$ of the strain between the cool state and the hot state is equal to the maximum recoverable strain $\int_0^1 \varepsilon^{tr}(s)ds$.

3.3. Shape memory cycle

In this section we provide closed-form expressions of the material response during the shape memory cycle, i.e. when the material is cooled down, deformed in a cooled

state and subsequently heated in a stress-free state.

3.3.1. Stress-free cooling We consider a stress-free initial state at high temperature, in which the material is fully austenitic. The stress-free material is then submitted to a decreasing temperature T. As a special case of the thermal loading studied in Sect.3.2.1, we have $\theta_0 = \theta_1 = 0$ as long as $\lambda(T) > -G_0$. When $\lambda(T)$ reaches the critical value $-G_0$, the volume fraction $\theta_0(s)$ starts to increase. For $\lambda(T) < -G_0$, we have $\theta_0(s) = c(s)$ i.e. the material is fully transformed in self-accommodated martensite. Note by (1) that there is no macroscopic deformation during the phase transformation. The behavior provided by the model is thus consistent with the experimental observations on martensitic transformation during stress-free cooling. We note that taking $G_0 < G_1$ is necessary to ensure that this consistency is respected.

3.3.2. Traction in the cooled state Consider now that the material is cooled down to a temperature T such that $\lambda(T) < -G_0$. From that point, the temperature is kept constant and an increasing strain ε is applied. It is expected that the volume fraction $\theta_0(s)$ decreases and that $\theta_1(s)$ increases with the applied strain, i.e. that reorientation of martensite occurs. The incremental problem (34) thus specializes as

$$\inf_{\theta_0,\theta_1} w(\varepsilon, T, \theta_0, \theta_1) + \int_0^1 -G_0\theta_0(s) + G_1\theta_1(s)ds \tag{58}$$

Let F be the functional to be minimized in (58). Since $\lambda(T) < G_0$, it can easily be verified that $F(\varepsilon, c - \theta_1, \theta_1) < F(\varepsilon, \theta_0, \theta_1)$ for any positive (θ_0, θ_1) such that $\theta_0 - \theta_1 < c$.The problem (58) thus reduces to

$$\inf_{0\leq\theta_1(s)\leq c(s)} w(\varepsilon, T, c - \theta_1, \theta_1) + \int_0^1 -G_0(c(s) - \theta_1(s)) + G_1\theta_1(s)ds \tag{59}$$

i.e. the minimization is restricted to fully martensitic states. The problem (59) is almost identical to the incremental problem (46) obtained for traction at high temperature, so that the solution to (59) is easily adapted from (47). We obtain

$$\begin{cases} \varepsilon = \dfrac{\sigma}{E} & \text{for } 0 \leq \sigma \leq \frac{G_0+G_1}{\varepsilon^{tr}_{max}} \\ \varepsilon = \dfrac{\sigma}{E} + \displaystyle\int_{\varepsilon^{tr}_{max}}^{\frac{G_0+G_1}{\sigma}} f'(x)c(f(x))xdx & \text{for } \frac{G_0+G_1}{\varepsilon^{tr}_{max}} \leq \sigma \leq \frac{G_0+G_1}{\varepsilon^{tr}_{min}} \\ \varepsilon = \dfrac{\sigma}{E} + \displaystyle\int_{\varepsilon^{tr}_{max}}^{\varepsilon^{tr}_{min}} f'(x)c(f(x))xdx & \text{for } \frac{G_0+G_1}{\varepsilon^{tr}_{min}} \leq \sigma \end{cases} \tag{60}$$

In contrast with the case of a high temperature, the stress-strain curve at low temperature is the same for all values of T (provided that $\lambda(T) < -G_0$). Eq. (60) gives the stress-strain curve during loading, i.e. for increasing values of the strain ε. Let θ_1^{max} be the value of θ_1 at the end of the loading, i.e. when the applied strain ε reaches its maximum value ε^{max}. If the applied strain is subsequently decreased while keeping the wire under traction ($\sigma \geq 0$), it can be verified that the unloading is elastic. In particular, when the material reaches its stress-free state, there remains a residual strain given by $\int_0^1 \theta_1^{max}(s)\varepsilon^{tr}(s)ds$.

3.3.3. Heating in the stress-free state Starting from the stress-free state given by (60), we now assume that the material is heated. The equations of evolutions are similar to those obtained in Sect. 3.3.1 and can be solved in a similar manner. We obtain that

$$\begin{cases} \theta_0 = c - \theta_1^{max}, \theta_1 = \theta_1^{max} & \text{for } \lambda(T) \leq G_0 \\ \theta_0 = 0, \theta_1 = \theta_1^{max} & \text{for } G_0 \leq \lambda(T) \leq G_1 \\ \theta_0 = \theta_1 = 0 & \text{for } G_1 \leq \lambda(T) \end{cases} \tag{61}$$

For high temperature ($G_1 \leq \lambda(T)$), the material is fully transformed in austenite.

4. Experimental validation

In this Section are reported some results of three types of experimental tests: a differential scanning calorimetry (DSC) test, mechanical traction tests at fixed temperature, and thermal cyclings at fixed stress. All those tests have been performed on a straight annealed 0.5mm diameter Nickel-Titanium wire, supplied by Memry Corp. (USA). The investigated alloy is $Ni_{50.4}Ti_{49.6}$ (at.%). We use the experimental results to discuss the identification of the model parameters as well as the validity of the model.

4.1. Calorimetry

A DSC test has first been carried out in order to identify the model parameters T_0 and λ_0 in (4). Phase transition temperatures and enthalpies of transition have been measured. The test equipment was a DSC 250 (TA Instruments). The DSC experiments were performed at a 10 K per minute temperature variation speed, under an inert Nitrogen environment (purge gas). A 7.9 mg sample of a 0.5mm diameter

virgin Ni-Ti wire has been tested. The test has been performed as detailed in Table 3.

Table 3. Experimental protocol

1	Test start at 293 K ; Heating up to 523 K (austenitic initial state)
2	Cooling down to 183 K ; Re-heating up to 523 K (first DSC cycle)
3	Cooling down to 183 K ; Re-heating up to 523 K (second DSC cycle)

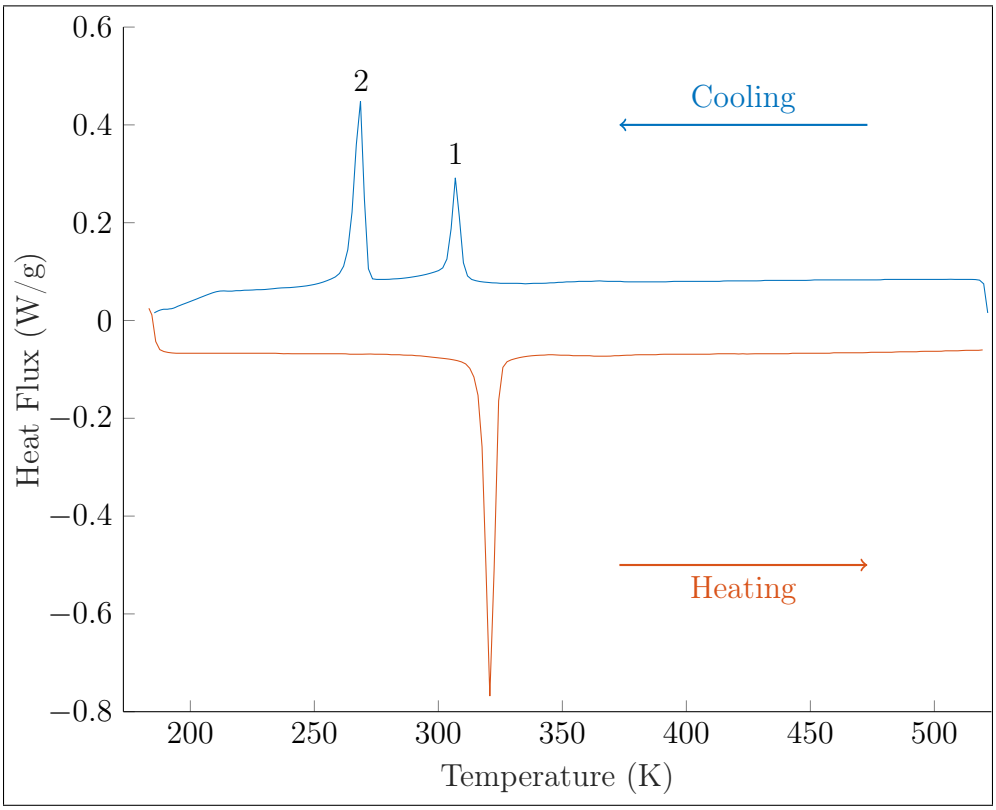

Figure 5. DSC test

The DSC chart is represented in Figure 5. The measured values are listed in Table 4. Two peaks are observed during cooling. Peak 1 (around 313 K) corresponds to the Austenite to R-phase transformation. Peak 2 (around 268 K) corresponds to the R-phase to Martensite transformation [23]. During heating, a single peak,

representing the Martensite to Austenite transformation, is observed. We choose not to model the R-phase here, because it tends to disappear under stress [24]. In this study, mechanical tests were always be performed on samples which had previously been heated up to 373 K and then cooled down to 253 K, in order to ensure that the material was in a martensitic state without R-phase at the beginning of the mechanical loading.

Table 4. DSC : Measured values

Peak	**Temperature**	**Enthalpy**
Formation of martensite	268.6 K	11.5 J/g
Formation of austenite	321.3 K	22.9 J/g

Using the results of Sect. 3.2.1 with the expression (4) of the latent heat, the phase transformation temperatures at zero stress are :

$$\begin{aligned} T^A &= T_0 - \frac{T_0 G_0}{\lambda_0} \qquad (\textit{cooling}) \\ T^B &= T_0 + \frac{T_0 G_0}{\lambda_0} \qquad (\textit{heating}) \end{aligned} \tag{62}$$

It follows that

$$T_0 = \frac{1}{2}(T^A + T^B) \tag{63}$$

Using Eq. (63) with the values of T^A and T^B reported in Table 4 yields $T_0 = 294.9$ K. In (4), the parameter λ_0 represents the volumic phase transformation enthalpy. We choose to measure it experimentally from the mass phase transformation enthalpy on the martensite formation peak at low temperature. Adopting a density of $\rho = 6.45$ mg/mm^3 for Nickel-Titanium [25], we obtain $\lambda_0 = 11.5 \times 6.45\,10^{-3}$ J.mm^{-3} = 74.2 MPa .

4.2. Traction tests under controlled temperature

Performing traction tests on SMA wires requires a careful experimental design. The phase transformation indeed induces some self-heating, so thermal conditions and loading rate strongly influence the results. For this reason, a specific testing chamber has been set up in order to perform the traction tests in water, with

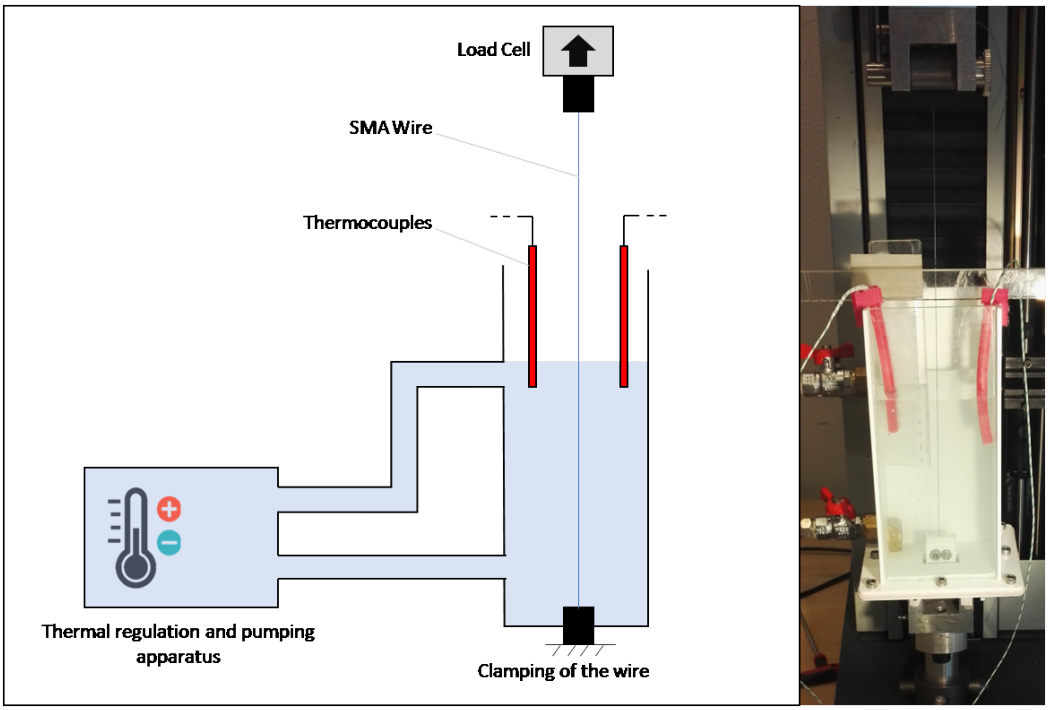

Figure 6. Experimental setup for mechanical tests at a controlled temperature

a strain measurement by Digital Image Correlation (DIC). The testing chamber is made of PMMA and contains a volume of water which is pumped into the chamber by a heating and cooling apparatus (see Figure 6) and goes out by overflow. The tested part of the wire finds is immersed in water, and its upper end is clamped on a displacement controlled ADAMEL DY31 testing machine. Two type K thermocouples monitor the water temperature at two different locations inside the water volume. The force in the wire was recorded using a 100N load cell and the local deformation in the wire was measured by DIC on images acquired by a Pike F421B camera (Allied Vision Technologies). A Matlab routine has been set up to record simultaneously the deformation images and the force values.

We set up the applied strain rate to remain reasonably low (10^{-4} s^{-1}) in order to minimize temperature changes in the wire. This value is often found in the literature on SMA [26] and can be justified from thermomechanical simulations [27]. The experimental protocol described allows us to approximate isothermal conditions: the

temperature in the wire is considered as uniform and equal to the water temperature.

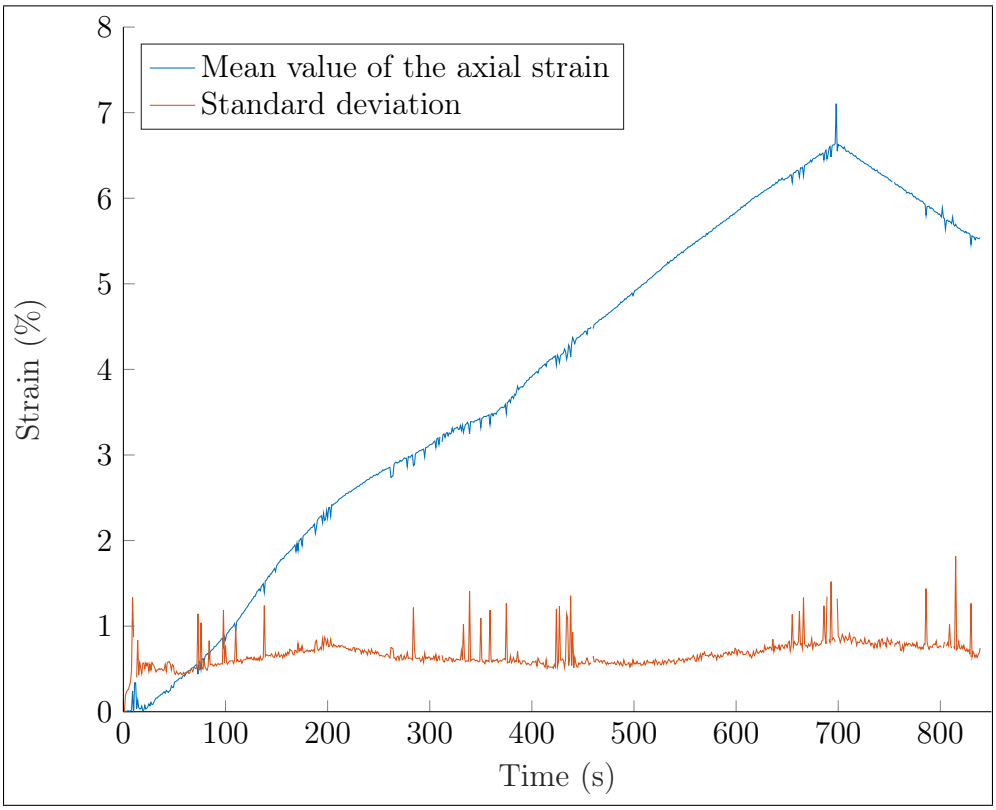

Figure 7. Homogeneous strain in the wire during phase transformation

The first traction tests performed on a virgin SMA wire usually do not exhibit a homogeneous strain: some localization is observed. In order to reach a stabilized thermomechanical behavior, the tested wire was submitted to 20 cycles of traction loading up to 30 N followed by unloading and heating. Before the first cycle and between each of those 20 cycles, the wire was unloaded and heated up to 373 K in a furnace with no imposed stress. It was then cooled down to 253 K, in order to reach self-accommodated martensite state with no R-phase at the beginning of the next cycle. After that 'training' procedure, the resulting stress-strain curve was found to be reproducible. Accordingly, a homogeneous strain was observed along the wire as illustrated in Figure 7 showing the average axial strain and the corresponding standard deviation of the axial strain field on the wire. This data has been obtained with the software GOM Correlate. As can be observed in Figure 7, the strain field

is homogeneous during the whole experiment, including phase transformation.

An example of stabilized stress-strain curve is shown in Fig. 9 at 298 K. Assuming that the test temperature is sufficiently low for the condition $\lambda(T) < G_0$ to be fulfilled, the stress-strain curve predicted by the model is given by Eq (60). It notably depends on the material parameters E, G_0+G_1, $\varepsilon^{tr}(s)$, $c(s)$, the identification of which is now discussed.

Consistently with Eq. (60), we first observe that the modulus E can be identified from the slope at the beginning of the curve, yielding $E = 28000$ MPa. Regarding the density $c(s)$ and the function $\varepsilon^{tr}(s)$, we make use of some background information on the texture of NiTi wires. Such wires indeed show an oriented *fiber texture* in which the $\langle 111 \rangle$ crystallographic direction in each grain is along the axis of the wire [28, 29, 30]. A perfect fiber texture would correspond to a constant function $\varepsilon^{tr}(s)$. In a true specimen, the $\langle 111 \rangle$ direction in most grains is not perfectly aligned with the axis of the wire. Moreover, there can be a small fractions of grains whose $\langle 111 \rangle$ direction differ significant from the axis wire. Recalling that the function ε^{tr} is decreasing, the function ε^{tr} in a true specimen is expected to be qualitatively of the shape depicted in Fig. 8, i.e with an almost flat plateau in its central part (stemming from a privileged orientation in the polycrystal) and larger fluctuations near $s = 0$ and $s = 1$. To model such a texture, we adopt the parameterized expression

$$\varepsilon^{tr}(s) = (\varepsilon^{tr}_{max} - \varepsilon^{tr}_{min}) \left(\frac{1 - \tanh(\beta(\tan(\pi(s^\gamma - \frac{1}{2}))))}{2} \right) + \varepsilon^{tr}_{min} \tag{64}$$

where $(\beta, \gamma) \in \mathbb{R}^2_+$. The functions ε^{tr} in (64) is monotonically decreasing and varies from ε^{tr}_{max} to ε^{tr}_{min} as s varies from 0 to 1. The parameters β et γ in (64) control the length and the slope of the central part. The function shown in (8) correspond to Eq. (64) with the parameters β and γ set to 0.02 and 1, respectively. The value $c(s) = 1$ is adopted.

Applying Eq (60) for calculating the stress-strain response of the model requires the expression of the inverse function of ε^{tr} and its derivative. To that purpose, we note that the inverse function of $\varepsilon^{tr}(s)$ in (64) is :

$$f(x) = \left[\frac{1}{2} + \frac{1}{\pi} \arctan \left(\frac{1}{\beta} \operatorname{arctanh} \left(1 - 2 \left(\frac{x - \varepsilon^{tr}_{min}}{\varepsilon^{tr}_{max} - \varepsilon^{tr}_{min}} \right) \right) \right) \right]^{\frac{1}{\gamma}} \tag{65}$$

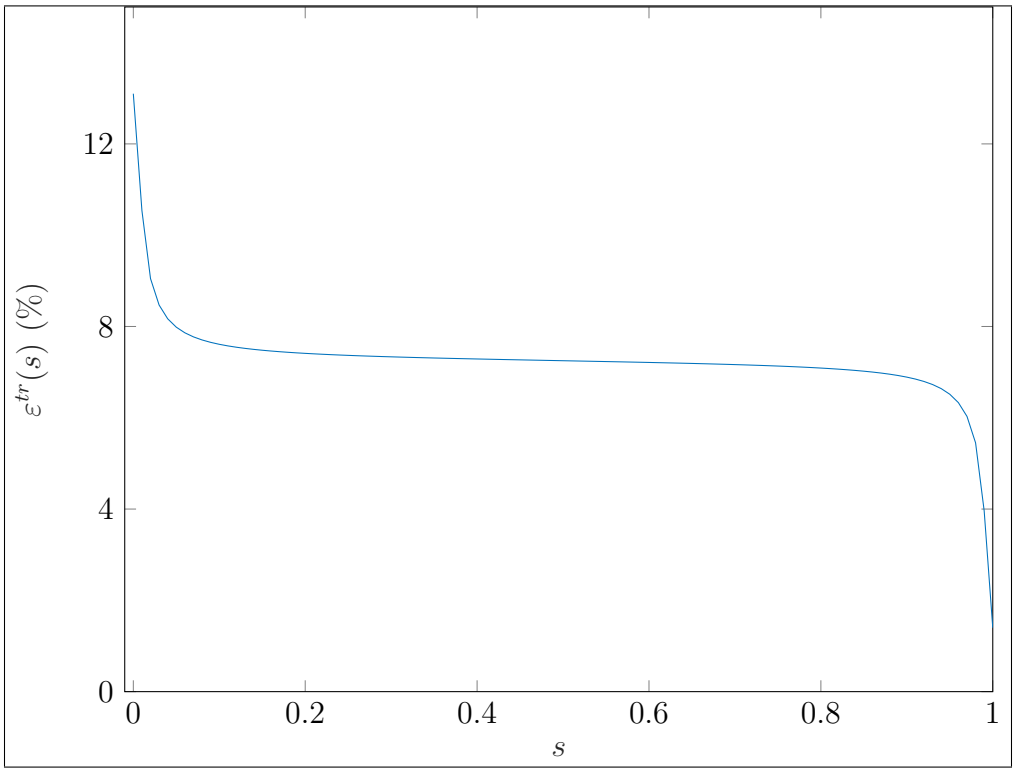

Figure 8. Example of function ε^{tr} corresponding to a non perfect fiber texture.

Setting

$$H(x) = \operatorname{arctanh}\left(1 - 2\left(\frac{x - \varepsilon^{tr}_{min}}{\varepsilon^{tr}_{max} - \varepsilon^{tr}_{min}}\right)\right), \tag{66}$$

we have

$$f'(x) = \frac{\beta}{2\gamma\pi}\left[\frac{1}{2} + \frac{1}{\pi}\arctan\left(\frac{H(x)}{\beta}\right)\right]^{\frac{1}{\gamma}-1} \frac{1}{(\varepsilon^{tr}_{min} - x)(\beta^2 + H(x)^2)} \frac{1}{1 - \left(\frac{x-\varepsilon^{tr}_{min}}{\varepsilon^{tr}_{max}-\varepsilon^{tr}_{min}}\right)} \tag{67}$$

Adopting (64), the function ε^{tr} is determined from 4 scalar parameters. In principle, ε^{tr}_{min} and ε^{tr}_{max} can be obtained from the crystallographic theory of martensite. This calculation, reported in Appendix B, gives $\varepsilon^{tr}_{max} = 0.107$ and $\varepsilon^{tr}_{min} = 0.024$. According to Eq. (60), the threshold stress for the beginning of phase transformation is $(G_0 + G_1)/\varepsilon^{tr}_{max}$. By tracking the end of linearity at the

beginning of the stress-strain curve, it is thus possible to identify $G_0 + G_1$. For the isothermal traction shown in Figure 9, the linear elastic domain ends for the stress $\sigma^{lin} = 50$ MPa, yielding $G_0 + G_1 = \sigma^{lin}\varepsilon^{tr}_{max} = 5.35$ MPa.

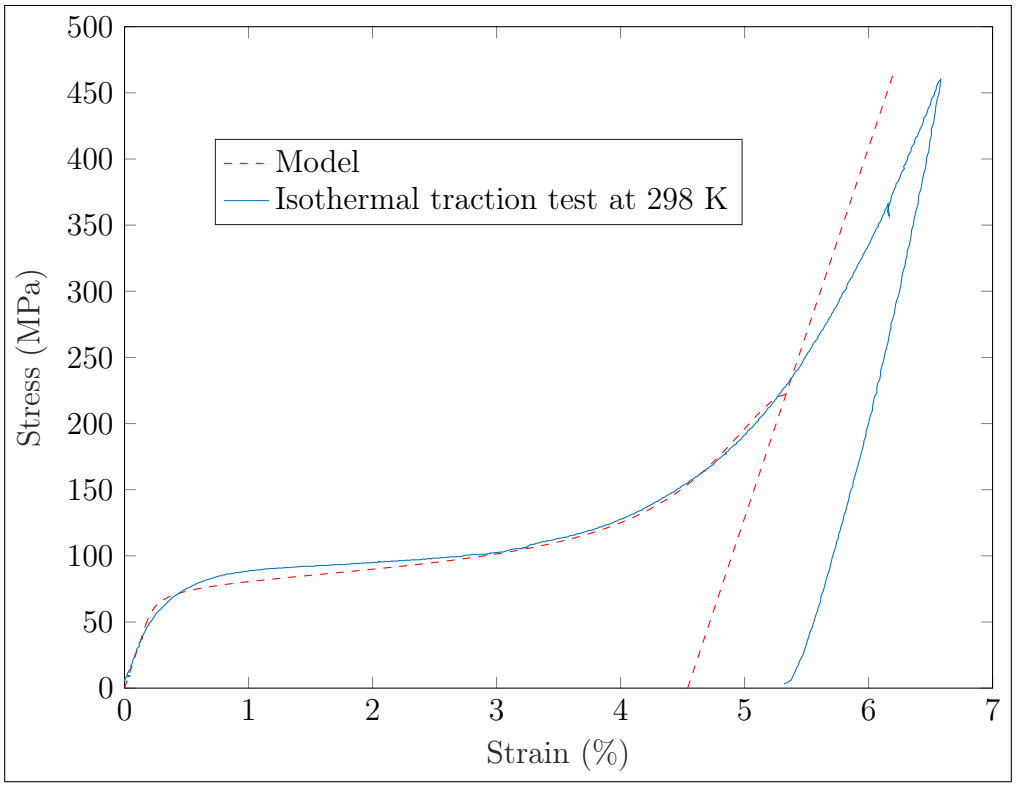

Figure 9. Model parameter identification - Texture C - Isothermal traction test at 298 K

The texture parameters β and γ are identified by trial and error, seeking for the best fit between the experimental curve and the analytical solution. The obtained parameters for this NiTi wire are listed in Table 5. The corresponding texture is labelled as texture C, and the resulting curve is plotted in Figure 9. A good fit is obtained for strains up to $\varepsilon = 5\%$. However, the predicted phase transformation ends for about $\varepsilon = 5\%$: beyond that value, the model gives a linear elastic behavior. This is in contradiction with the experiments, which show that phase transformation still takes place for strains up to 6.5% (this is indicated by the fact that the experimental loading and unloading curves do not overlap in the high strain domain). This discrepancy between the model curve and the experimental curve partially stems

from the elastic interaction between the grains, which has not been considered in the model.

Table 5. Model parameter identification - Texture C

E	28000	MPa
λ	74.2	MPa
T_0	294.9	K
ε^{tr}_{min}	0.024	
ε^{tr}_{max}	0.107	
β	0.3	
γ	0.32	
G_0	3	MPa
G_1	3.5	MPa

An attempt at obtaining a better fit between the analytical curve and the experimental curve has been made by relaxing the parameters ε^{tr}_{min} and ε^{tr}_{max}: instead of using the values provided by the crystallographic theory, we consider ε^{tr}_{min} and ε^{tr}_{max} as free parameters. This allows to get a better fit with the experimental curve, especially in the high strains domain as shown in Figure 10. The material parameters of the corresponding texture (labelled as texture C*) are listed in Table 6.

Table 6. Model parameter identification - Texture C*

E	28000	MPa
λ	74.2	MPa
T_0	294.9	K
ε^{tr}_{min}	0.014	
ε^{tr}_{max}	0.131	
β	0.25	
γ	0.35	
G_0	3	MPa
G_1	3.5	MPa

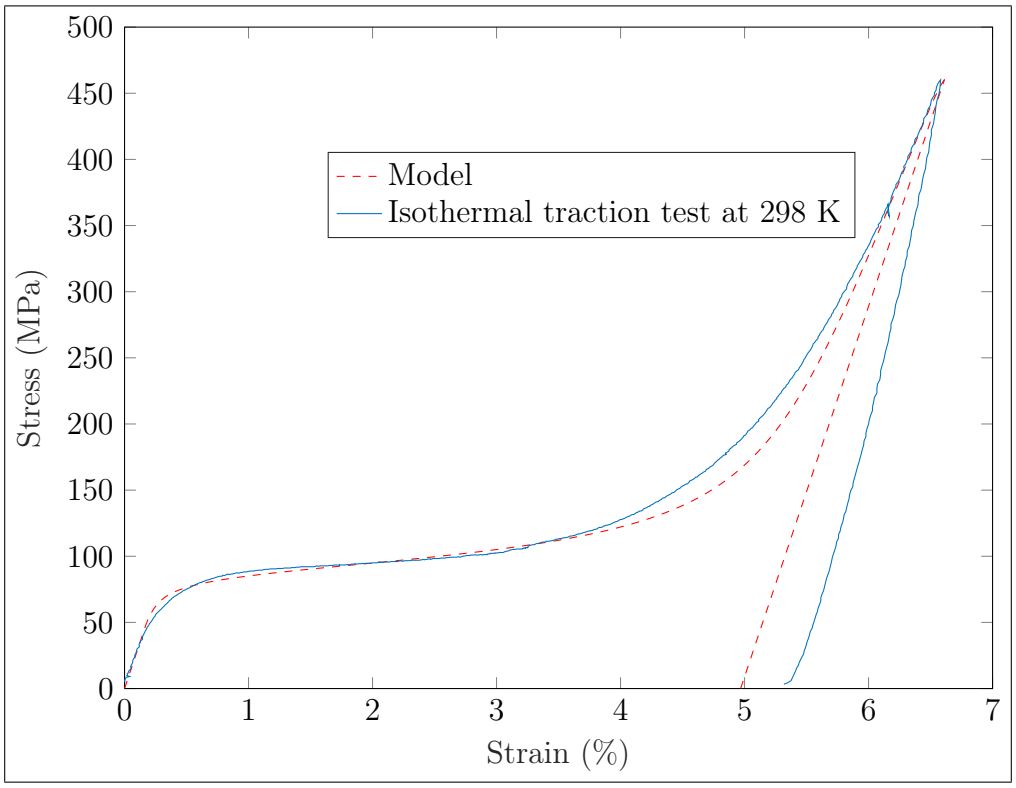

Figure 10. Model parameter identification - Texture C* - Isothermal traction test at 298 K

In Figure 11 is plotted the function $\varepsilon^{tr}(s)$ for texture C*. With texture C*, most transformation strains are found to fall between 4 and 7 %. This can be interpreted as the result of a privileged grain orientation in the wire. It is insightful to interpret the model stress-strain response in Fig. 10 in terms of the corresponding distribution of transformation strains shown in Figure 11. Firstly, the rounded part at the end of the linear elastic portion corresponds to the transformation of the grains parametrized by s close to 0. They are very favorably oriented with respect to the loading axis and transform first. Secondly, the stress-strain curve features an almost flat plateau, which corresponds to the transformation of the predominant grains with transformation strains in the range 4–7%. Finally, the end of the stress-strain curve features a significant nonlinear hardening, corresponding to the phase transformation of the less favorably oriented grains in the polycrystal. These grains present a low $\varepsilon^{tr}(s)$ value.

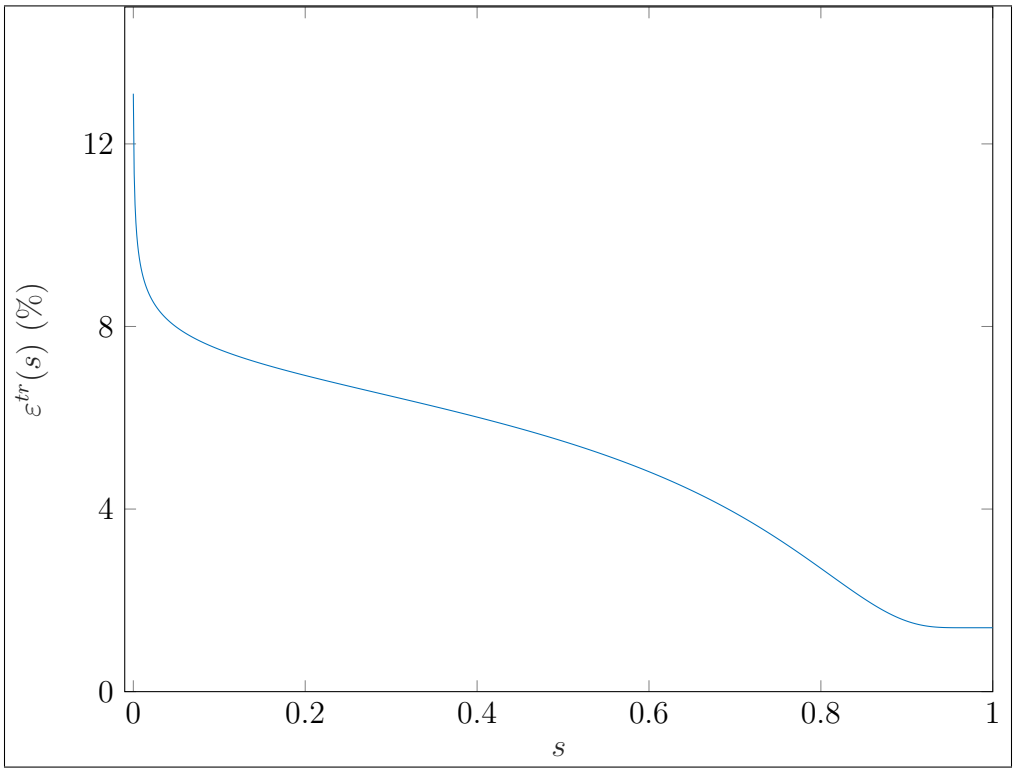

Figure 11. Function $\varepsilon^{tr}(s)$ for the texture C*.

Compared to texture C, the function $\varepsilon^{tr}(s)$ corresponding to texture C* yields a better match with the experimental results, but it probably deviates more from the real texture of the material. This all falls down to the simplified form of the free energy (3): Allowing the function ε^{tr} to deviate from the real texture partially makes up for the fact that modeled energy does not exactly correspond to the true energy of the material.

4.3. Thermal cycling under constant stress

At this point, all the material parameters have been identified, except for G_0 and G_1. More precisely, the sum $G_0 + G_1$ is known but the value of G_0 (and consequently G_1) is not known. Its value can be obtained from thermal cyclic under constant stress, as is now explained. The SMA wire is mechanically loaded in the testing chamber at a water temperature of 358 K, up to a traction stress of 127 MPa (25N). This

stress is then maintained constant in time with the help of a PID controller included in the TestWorks software, which is used to control the electromechanical machine. Thermal loadings were carried out by varying the water temperature in the testing chamber between 283 and 363 K.

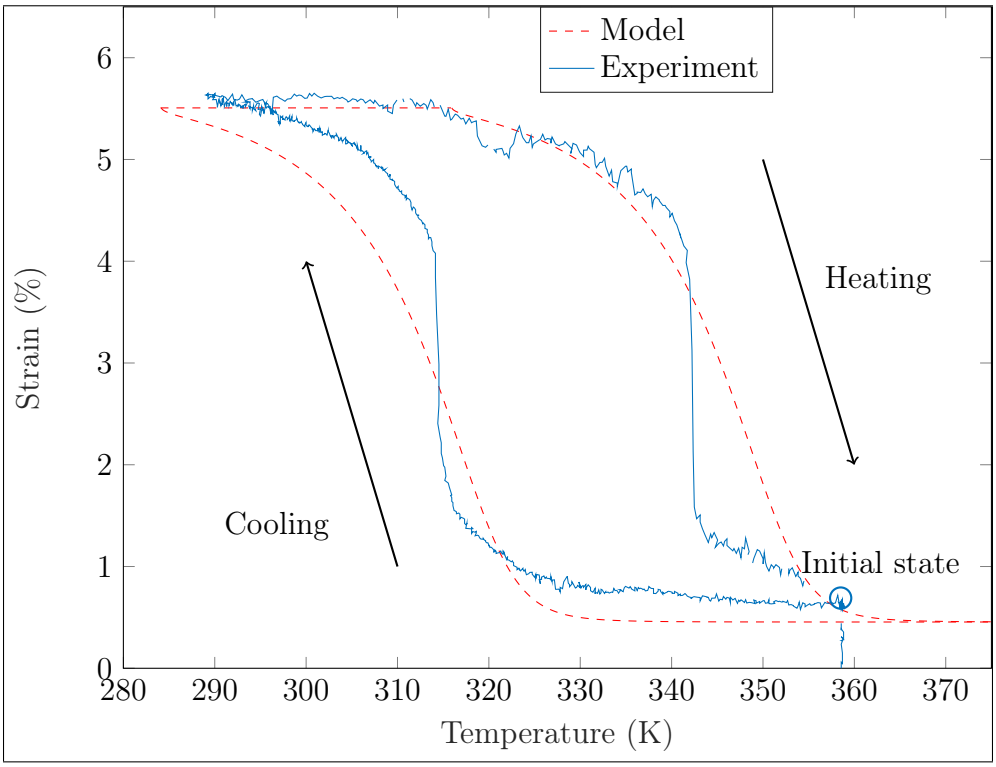

Figure 12. Thermal cycle at a constant stress $\sigma = 127$ MPa.

In Figure 12, the experimentally measured strain in the wire is plotted as a function of the water temperature. We can now calculate the parameter G_1 by measuring the temperature difference ΔT between the heating and the cooling curve at a fixed strain. Using equations (52) and (56) as well as the expression (4) of the latent heat, we have indeed

$$\Delta T = \frac{2G_1 T_0}{\lambda_0}.$$

For $\varepsilon = 0.03$, we measure $\Delta T = 27.8$ K which leads to $G_0 = 3.0$ MPa and $G_1 = 3.5$ MPa. We can note that the condition $G_0 < G_1$ introduced in Sect. 2.2 is fulfilled. Moreover, with the values obtained in Sect. 4.1 for λ_0 and T_0, the condition

$\lambda(T) < G_0$ is satisfied at 298 K. This justifies using Eq. (60) to plot the stress-strain curve. All model parameters are now identified, and the analytical solution for thermal cycling, established in Eqs. (51), (53), (55) and (56), is plotted in Figure 12. That curve is in relatively good agreement with the experimental results, which contributes to validate the model.

4.4. Superelastic regime

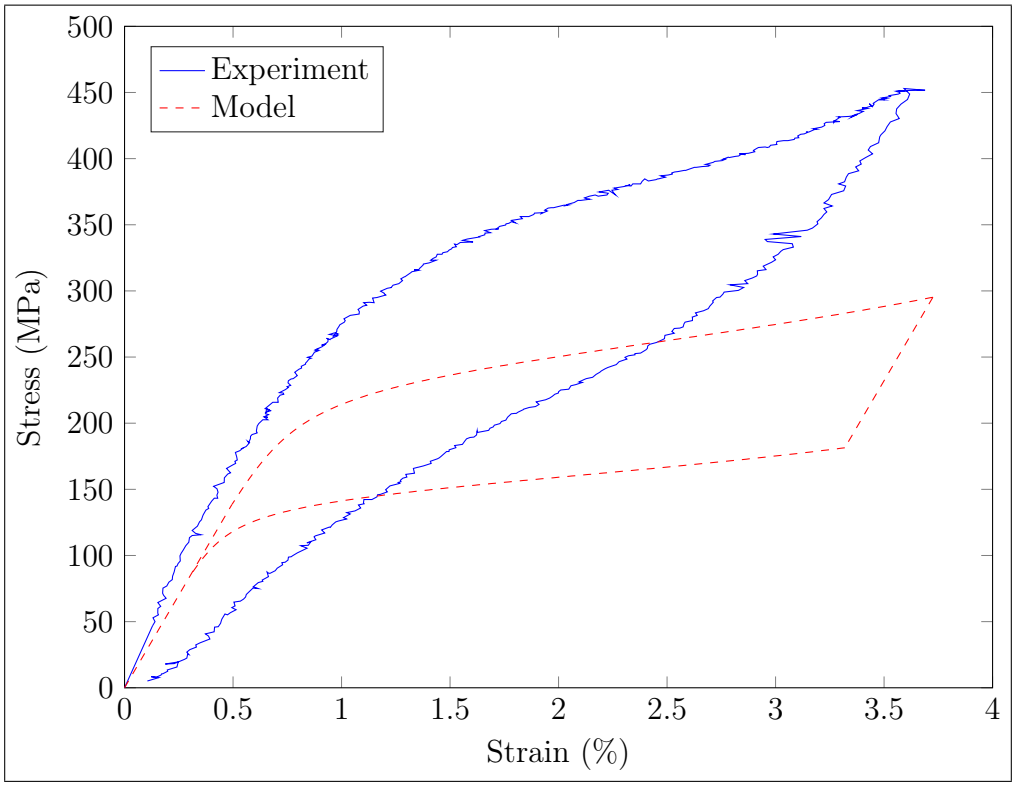

Figure 13. Texture C* - Isothermal traction test at 353 K

In Fig. 13(solid line) is plotted the experimental stress-strain curve obtained at 353 K (which is about the maximum temperature that can applied in the designed testing chamber). At such temperature, the material enters the superelastic regime. The stress-strain curve for texture C* is shown in dashed line. There is clearly a discrepancy between the experimental curve and the curve corresponding to texture C*. This is not entirely surprising because the martensitic microstructures that

appear in the superelastic regime are much different from those that appear in the low temperature regime. It could be possible to identify a function $\varepsilon^{tr}(s)$ that would yield a good fit at high temperature, but then the corresponding fit at low temperature would be poor. This is a limitation of the model: using a single function $\varepsilon^{tr}(s)$ is probably not sufficient to describe accurately the nonlinear phase-transformation hardening at all temperatures.

5. Conclusion

The proposed model is based on a three-dimensional micromechanical expression for the free energy, using the wire geometry to perform some simplifications. In particular, the internal variables are reduced to two scalars per orientation (corresponding to the volume fractions of self-accommodated martensite and oriented martensite). Such simplifications allows analytical solutions to be obtained for the material response under typical loadings of interest. The obtained solutions depend on the polycrystalline texture through the functions c and ε^{tr} representing the volumic density of crystalline orientations and the distribution of transformation strain, respectively. The identification of the material parameters have been discussed in detail and can take advantage of the presented analytical solutions. The model could be used for designing SMA actuators. Although a satisfactory fit with the experiments is obtained for the loadings corresponding to the shape memory effect (traction at low temperature, thermal cycling a constant stress), it would be interesting to refine the model by taking the elastic interaction between the grains into account. This would typically result in an additional term in the free energy. It would also be interesting to improve the model by using different elastic moduli for the austenite and the martensite. We also note that the proposed model could be extended to SMA rods (loaded in traction and compression) by adding an additional internal variable representing the volume fractions of the most favorably martensitic variant in compression.

6. Acknowledgments

This work has been partially funded by Arcora (Ingérop Group), and by ANRT under CIFRE grant No 2015/0495. The authors wish to thank Karim Benzarti who performed the DSC experiment, and Christophe Bernard who manufactured

the experimental traction chamber.

Appendix A. Variational principle for monotonic evolution

We denote by $v(f)$ the sign of variation of a given monotone function f, i.e. $v(f) = 1$ if f is increasing and $v(f) = -1$ if f is decreasing. For a given history $(\varepsilon(t), T(t))$ on a time interval $[0, \tau]$, we are interested in finding a solution to the evolution equation (33) such that $\theta_i(s,t)$ is monotonic in time and $v(\theta_i(s,.) = \epsilon_i(s)$ where $\epsilon_i(s) \in \{-1, 1\}$ is given. To that purpose, for any t in $[0, \tau]$, consider a solution $\tilde{\theta}_i(s,t)$ to the minimization problem

$$\inf_{\theta_0,\theta_1} w(\varepsilon(t), T(t), \theta_0, \theta_1) + \int_0^1 G_0\epsilon_0(s)\theta_0(s) + G_1\epsilon_i(s)\theta_1(s)ds \tag{A.1}$$

If $\tilde{\theta}_i(s,t)$ satisfies $v(\tilde{\theta}_i(s,.)) = \epsilon_i(s)$, we claim that $\tilde{\theta}_i(s,t)$ is a solution to the evolution problem defined by Eqs (30), (32) and (33). For any fixed t, the stationarity conditions in (A.1) indeed read as $0 \in \partial w + (\epsilon_0 G_0, \epsilon_1 G_1) + \partial I_{\mathcal{T}}$ i.e.

$$\begin{aligned} 0 &= -\lambda(T) + \epsilon_0(s)G_0 + z(s) - a_0(s) \\ 0 &= \sigma\varepsilon^{tr}(s) - \lambda(T) + \epsilon_1(s)G_1 + z(s) - a_1(s) \end{aligned} \tag{A.2}$$

where $(z(s), a_0(s), a_1(s))$ are submitted to conditions (32). Let $B_i^d(s) = \epsilon_i(s)G_i$. Since $v(\tilde{\theta}_i(s,.)) = \epsilon_i(s)$, the value $B_i^d(s)$ thus defined satisfies (30). Hence (A.2) can be rewritten as

$$\begin{aligned} 0 &= -\lambda(T) + B_0^d(s) + z(s) - a_0(s) \\ 0 &= \sigma\varepsilon^{tr}(s) - \lambda(T) + B_1^d(s) + z(s) - a_1(s) \end{aligned} \tag{A.3}$$

where $(z(s), a_0(s), a_1(s))$ and $B_i^d(s)$ satisfies the conditions (32) and (30). The evolution equation (33) is thus satisfied at each time, which proves the claim.

A similar result can be obtained for stress-driven loading by replacing the Helmoltz free energy w with the Gibbs free energy w_* in the reasoning.

Appendix B. Transformation strains in NiTi

NiTi alloys obey a cubic to monoclinic-I phase transformation. In such case, there are 12 martensitic variants with transformation strains listed in Table B1. Values of the lattice parameters for $NiTi_{49.75}$ alloys are $\alpha = 0.0234$, $\beta = -0.0437$, $\delta = 0.058$, $\epsilon = 0.0426$ [31].

Table B1. Cubic to monoclinic-I transformation

$\mathbf{e}_1^{tr}$	$\mathbf{e}_2^{tr}$	$\mathbf{e}_3^{tr}$	$\mathbf{e}_4^{tr}$
$\begin{pmatrix} \alpha & \delta & \epsilon \\ \delta & \alpha & \epsilon \\ \epsilon & \epsilon & \beta \end{pmatrix}$	$\begin{pmatrix} \alpha & \delta & -\epsilon \\ \delta & \alpha & -\epsilon \\ -\epsilon & -\epsilon & \beta \end{pmatrix}$	$\begin{pmatrix} \alpha & -\delta & -\epsilon \\ -\delta & \alpha & \epsilon \\ -\epsilon & \epsilon & \beta \end{pmatrix}$	$\begin{pmatrix} \alpha & -\delta & \epsilon \\ -\delta & \alpha & -\epsilon \\ \epsilon & -\epsilon & \beta \end{pmatrix}$
$\mathbf{e}_5^{tr}$	$\mathbf{e}_6^{tr}$	$\mathbf{e}_7^{tr}$	$\mathbf{e}_8^{tr}$
$\begin{pmatrix} \alpha & \epsilon & \delta \\ \epsilon & \beta & \epsilon \\ \delta & \epsilon & \alpha \end{pmatrix}$	$\begin{pmatrix} \alpha & -\epsilon & \delta \\ -\epsilon & \beta & -\epsilon \\ \delta & -\epsilon & \alpha \end{pmatrix}$	$\begin{pmatrix} \alpha & -\epsilon & -\delta \\ -\epsilon & \beta & \epsilon \\ -\delta & \epsilon & \alpha \end{pmatrix}$	$\begin{pmatrix} \alpha & \epsilon & -\delta \\ \epsilon & \beta & -\epsilon \\ -\delta & -\epsilon & \alpha \end{pmatrix}$
$\mathbf{e}_9^{tr}$	$\mathbf{e}_{10}^{tr}$	$\mathbf{e}_{11}^{tr}$	$\mathbf{e}_{12}^{tr}$
$\begin{pmatrix} \beta & \epsilon & \epsilon \\ \epsilon & \alpha & \delta \\ \epsilon & \delta & \alpha \end{pmatrix}$	$\begin{pmatrix} \beta & -\epsilon & -\epsilon \\ -\epsilon & \alpha & \delta \\ -\epsilon & \delta & \alpha \end{pmatrix}$	$\begin{pmatrix} \beta & -\epsilon & \epsilon \\ -\epsilon & \alpha & -\delta \\ \epsilon & -\delta & \alpha \end{pmatrix}$	$\begin{pmatrix} \beta & \epsilon & -\epsilon \\ \epsilon & \alpha & -\delta \\ -\epsilon & -\delta & \alpha \end{pmatrix}$

Adopting the notations of Sect. 2, the uniaxial transformation strain $\varepsilon^{tr}(s)$ in orientation s is

$$\varepsilon^{tr}(s) = \max_{1\leq i\leq 12} \mathbf{n}\cdot\mathbf{R}(s)\mathbf{e}_i^{tr}\mathbf{R}(s)^T\cdot\mathbf{n} \tag{B.1}$$

where $\mathbf{R}(s)$ is the rotation corresponding to orientation s. It follows from (B.1) that

$$\varepsilon_{min}^{tr} \leq \varepsilon^{tr}(s) \leq \varepsilon_{max}^{tr}$$

where

$$\begin{aligned} \varepsilon_{min}^{tr} &= \min_{\mathbf{R}\in SO_3} \max_{1\leq i\leq 12} \mathbf{n}\cdot\mathbf{R}\mathbf{e}_i^{tr}\mathbf{R}^T\cdot\mathbf{n}, \\ \varepsilon_{max}^{tr} &= \max_{\mathbf{R}\in SO_3} \max_{1\leq i\leq 12} \mathbf{n}\cdot\mathbf{R}\mathbf{e}_i^{tr}\mathbf{R}^T\cdot\mathbf{n} \end{aligned} \tag{B.2}$$

The calculation of ε_{max}^{tr} can be done in closed-form. Swapping the order of the two maxima indeed yields

$$\varepsilon_{max}^{tr} = \max_{1\leq i\leq 12} \max_{\mathbf{R}\in SO_3} \mathbf{n}\cdot\mathbf{R}\mathbf{e}_i^{tr}\mathbf{R}^T\cdot\mathbf{n}$$

As $\mathbf{R}$ varies in SO_3, the vector $\mathbf{R}\cdot\mathbf{n}$ varies on the unit sphere $S_2 = \{\mathbf{m}\in\mathbb{R}^3 : \|\mathbf{m}\| = 1\}$. Hence $\varepsilon_{max}^{tr} = \max_i \max_{\mathbf{m}\in S_2} \mathbf{m}\cdot\mathbf{e}_i^{tr}\cdot\mathbf{m}$. For a given i, $\max_{\mathbf{m}\in S_2} \mathbf{m}\cdot\mathbf{e}_i^{tr}\cdot\mathbf{m}$ is equal to the maximum eigenvalue of $\mathbf{e}_i^{tr}$. The transformation strains listed in Table B1 all have the same maximum eigenvalue which can be expressed in terms of the

lattice parameters as $(\alpha+\beta+\delta+\sqrt{(\alpha-\beta+\delta)^2+8\epsilon^2})/2$. In conclusion, we have

$$\varepsilon^{tr}_{max} = \frac{1}{2}(\alpha+\beta+\delta+\sqrt{(\alpha-\beta+\delta)^2+8\epsilon^2})$$

For NiTi, we obtain $\varepsilon^{tr}_{max} \simeq 0.107$.

The calculation of ε^{tr}_{min} in (B.2) is tricky to perform in closed-form. Using numerical optimization to solve the min-max problem defining ε^{tr}_{min} yields $\varepsilon^{tr}_{min} \simeq 0.024$.

References

[1] F. Auricchio, R.L. Taylor, and J. Lubliner. Shape-memory alloys: macromodelling and numerical simulations of the superelastic behavior. *Computer Methods in Applied Mechanics and Engineering*, 146(3):281 – 312, 1997.

[2] J.G. Boyd and D.C. Lagoudas. A thermodynamical constitutive model for shape memory materials. part i. the monolithic shape memory alloy. *International Journal of Plasticity*, 1996.

[3] S Leclercq and Ch Lexcellent. A general macroscopic description of the thermomechanical behavior of shape memory alloys. *Journal of the Mechanics and Physics of Solids*, 44(6):953–980, 1996.

[4] Y. Chemisky, A. Duval, E. Patoor, and T. Ben Zineb. Constitutive model for shape memory alloys including phase transformation, martensitic reorientation and twins accommodation. *Mechanics of Materials*, 43(7):361 – 376, 2011.

[5] A.C. Souza, E.N. Mamiya, and N. Zouain. Three-dimensional model for solids undergoing stress-induced phase transformations. *European Journal of Mechanics - A/Solids*, 17(5):789 – 806, 1998.

[6] K. Tanaka, S. Kobayashi, and Y. Sato. Thermomechanics of transformation pseudoelasticity and shape memory effect in alloys. *International Journal of Plasticity*, 2(1):59–72, 1986.

[7] W. Zaki and Z. Moumni. A three-dimensional model of the thermomechanical behavior of shape memory alloys. *Journal of the Mechanics and Physics of Solids*, 55(11):2455–2490, 2007.

[8] M. Peigney, J.P. Seguin, and Eveline Hervé-Luanco. Numerical simulation of shape memory alloys structures using interior-point methods. *International Journal of Solids and Structures*, 48(20):pp. 2791–2799, 2011.

[9] G. Sagar and E. Stein. Contributions on the theory and computation of mono-and poly-crystalline cyclic martensitic phase transformations. *ZAMM-Journal of Applied Mathematics and Mechanics/Zeitschrift für Angewandte Mathematik und Mechanik*, 90(9):655–681, 2010.

[10] D. Bernardini and T. J. Pence. Models for one-variant shape memory materials based on dissipation functions. *International Journal of Non-Linear Mechanics*, 37(8):1299–1317, 12 2002.

[11] S. Govindjee and C. Miehe. A multi-variant martensitic phase transformation model: formulation and numerical implementation. *Computer Methods in Applied Mechanics and Engineering*, 191:215–238, 2001.

[12] S. Stupkiewicz and H. Petryk. Modelling of laminated microstructures in stress-induced martensitic transformations. *Journal of Mechanics Physics of Solids*, 50:2303–2331, 2002.

[13] F.A. Nae, Y. Matsuzaki, and T. Ikeda. Micromechanical modeling of polycrystalline shape-memory alloys including thermo-mechanical coupling. *Smart Materials and Structures*, 12(1):6, 2003.

[14] A. Kelly, A. P. Stebner, and K. Bhattacharya. A micromechanics-inspired constitutive model for shape-memory alloys that accounts for initiation and saturation of phase transformation. *Journal of the Mechanics and Physics of Solids*, 97(C), 2016.

[15] G. Song, Q.P. Sun, and H. Kehchic. Effect of microstructure on the hardening and softening behavIors of polycrystalline shape Memory alloys Part I: Micromechanics constitutive modeling. *Acta Mechanica Sinica*, 16:309–324, 2000.

[16] L. Anand and M. E. Gurtin. Thermal effects in the superelasticity of crystalline shape-memory materials. *Journal of Mechanics Physics of Solids*, 51:1015–1058, 2003.

[17] R. Abeyaratne, S. Kim, and J. Knowles. A one-dimensional continuum model for shape-memory alloys. *Int. J. Solids Struct.*, 31:2229–2249, 1994.

[18] K. Hackl and R. Heinen. A micromechanical model for pretextured polycrystalline shape-memory alloys including elastic anisotropy. *Continuum Mechanics and Thermodynamics*, 19(8):499–510, 2008.

[19] M. Peigney. A non-convex lower bound on the effective free energy of polycrystalline shape memory alloys. *J. Mech. Phys. Solids*, 57:970–986, 2009.

[20] M. Peigney. On the energy-minimizing strains in martensitic microstructures-part 1:geometrically nonlinear theory. *J. Mech. Phys. Solids*, 61:1489–1510, 2013.

[21] B. Halphen and Q.S. Nguyen. Sur les matériaux standard généralisés. *Journal de Mécanique*, 14:39–63, 1975.

[22] M. Frémond. *Non-Smooth Thermomechanics*. Physics and astronomy online library. Springer Berlin Heidelberg, 2001.

[23] T. W. Duerig and K. Bhattacharya. The influence of the r-phase on the superelastic behavior of niti. *Shape Memory and Superelasticity*, 1(2):153–161, 2015.

[24] T. W. Duerig, A. R. Pelton, and K. Bhattacharya. The measurement and interpretation of transformation temperatures in nitinol. *Shape Memory and Superelasticity*, 3(4):485–498, 2017.

[25] C.B. Churchill, J.A. Shaw, and M.A. Iadicola. Tips and tricks for characterizing shape memory alloy wire: Part 4 – thermo-mechanical coupling. *Experimental Techniques*, 34:63 – 80, 03 2010.

[26] K. Kim and S. Daly. Experimental studies of phase transformation in shape memory alloys. In Tom Proulx, editor, *Application of Imaging Techniques to Mechanics of Materials and Structures, Volume 4*, pages 267–269, New York, NY, 2013. Springer New York.

[27] M. Peigney and J.P. Seguin. An incremental variational approach to coupled thermo-mechanical probles in anelastic solids. application to shape memory alloys. *International*

Journal of Solids and Structures, 50:pp. 4043–4054, 2013.

[28] P. Thamburaja and L. Anand. Polycrystalline shape-memory materials: Effect of crystallographic texture. *Journal of the Mechanics and Physics of Solids*, 49(4):709–737, 4 2001.

[29] G. Laplanche, T. Birk, S. Schneider, J. Frenzel, and G. Eggeler. Effect of temperature and texture on the reorientation of martensite variants in niti shape memory alloys. *Acta Materialia*, 127:143 – 152, 2017.

[30] K. Bhattacharya. *Microstructure of Martensite: Why it Forms and how it Gives Rise to the Shape-memory Effect*. Oxford Series on Materials Modelling. OUP Oxford, 2003.

[31] K. Knowles and D. Smith. Crystallography of the martensitic transformation in equiatomic nickel-titanium. *Acta Materialia*, 29:101–110, 1981.